SANDIA REPORT

SAND2018-10945
Unlimited Release
Printed September 2018

Supersedes SAND2018-8603
Dated July 2018

A comparative study on wave prediction for WECs

Ryan G. Coe, Giorgio Bacelli, Victor Nevarez, Hancheol Cho, Felipe Wilches-Bernal

Prepared by
Sandia National Laboratories
Albuquerque, New Mexico 87185 and Livermore, California 94550

Sandia National Laboratories is a multi-mission laboratory managed and operated by Sandia Corporation, a wholly owned subsidiary of Lockheed Martin Corporation, for the U.S. Department of Energy's National Nuclear Security Administration under contract DE-AC04-94AL85000.

Issued by Sandia National Laboratories, operated for the United States Department of Energy by Sandia Corporation.

Available to DOE and DOE contractors from
U.S. Department of Energy
Office of Scientific and Technical Information
P.O. Box 62
Oak Ridge, TN 37831

Telephone: (865) 576-8401
Facsimile: (865) 576-5728
E-Mail: reports@adonis.osti.gov
Online ordering: http://www.osti.gov/bridge

Available to the public from
U.S. Department of Commerce
National Technical Information Service
5285 Port Royal Rd
Springfield, VA 22161

Telephone: (800) 553-6847
Facsimile: (703) 605-6900
E-Mail: orders@ntis.fedworld.gov
Online ordering: http://www.ntis.gov/help/ordermethods.asp?loc=7-4-0#online

SAND2018-10945
Unlimited Release
Printed September 2018

Supersedes SAND2018-8603
dated July 2018

A comparative study on wave prediction for WECs

Ryan G. Coe
Sandia National Laboratories
P.O. Box 5800, MS 1124
Albuquerque, NM 87185-9999
rcoe@sandia.gov

Giorgio Bacelli
Sandia National Laboratories
P.O. Box 5800, MS 1124
Albuquerque, NM 87185-9999
gbacell@sandia.gov

Victor Nevarez
Sandia National Laboratories
P.O. Box 5800, MS 1124
Albuquerque, NM 87185-9999
vnevare@sandia.gov

Hancheol Cho
Sandia National Laboratories
P.O. Box 5800, MS 1124
Albuquerque, NM 87185-9999
hancho@sandia.gov

Felipe Wilches-Bernal
Sandia National Laboratories
P.O. Box 5800, MS 1140
Albuquerque, NM 87185-9999
fwilche@sandia.gov

Acknowledgment

Sandia National Laboratories is a multi-mission laboratory managed and operated by National Technology and Engineering Solutions of Sandia, LLC., a wholly owned subsidiary of Honeywell International, Inc., for the U.S. Department of Energys National Nuclear Security Administration under contract DE-NA0003525. The views expressed in the article do not necessarily represent the views of the U.S. Department of Energy or the United States Government.

Contents

Appendix

List of Figures

List of Tables

Executive summary

The idea of acausality for control of a wave energy converter (WEC) is a concept that has been popular since the birth of modern wave energy research in the 1970s. This concept has led to considerable research into wave prediction and feedforward WEC control algorithms. However, the findings in this report mostly negate the need for wave prediction to improve WEC energy absorption, and favor instead feedback driven control strategies. Feedback control is shown to provide performance that rivals a prediction-based controller, which has been unrealistically assumed to have perfect prediction.

It is well known in classical control engineering that perfect knowledge of past and future events will always lead to higher performing systems. However, it is also well known that the underlying system must be well-designed; control cannot fix a bad design. Additionally, one must consider the practical application of a control design, which relies on measurements and actuation systems. There are major implications to cost and reliability when relying on remote sensors requiring real-time data-streaming (e.g., remote wave buoys). This report shows that for a well-designed WEC, in which closed loop dynamics is considered since early stages of design, a suboptimal controller using no prediction can achieve more than 90% of the theoretical maximum.

As shown in Figure 1, a predictionless feedback resonating (FBR) controller performs within 0.1% percent of a controller with perfect future knowledge (something which is not practically attainable). Given the major challenges with accurate and robust wave prediction, this result provides a major argument and incentive for utilizing feedback for WEC control. Implementation of these feedback strategies is readily attainable, while the strategy requiring perfect wave prediction will demand an unknown number of additional years to research and develop, all in the service of a marginal 1% benefit.

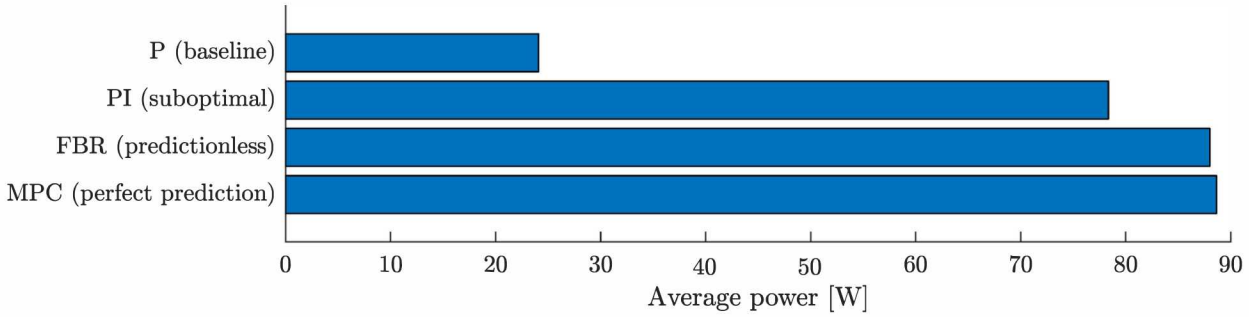

Figure 1: Summary of study results showing average power across model-scale sea states. A more detailed version of these results is presented in Table 2.1.

Chapter 1

Background

The idea of acausality for control of a wave energy converter (WEC) is concept that has been popular since the birth of modern wave energy research in the 1970s. This concept has two components: (A) that the excitation caused on a WEC by ocean waves is described by an acausal process (i.e., one must know the wave elevation at some time in the future to know the excitation force at the present time) and (B) that this acausality, in turn, requires that some prediction/forecasting/feedforward control be utilized for efficient WEC control. These concepts have led to considerable research into wave prediction and feedforward WEC control algorithms.

(A) The acausality of wave excitation
Taking first the idea of wave excitation as an acausal process, we can generally find quick agreement that Newtonian physics is always causal. Acausality is simply a matter of how you define (and therefore measure) the system. The common way of taking the wave elevation as input to a system which results in the exciting force is somewhat backwards. The excitation reaction on a floating body is due to the pressure on its hull which is a result of the fluid velocity. Thus, looking at the wave elevation as the input to the system is somehow similar to measuring a person's temperature with the impression that the temperature is the cause of their ailment, where it is in fact a symptom. In fact, if looking at the direct cause of the the excitation force on the buoy, which is the pressure, it is possible to see that the transfer function between pressure and force is causal [2].

(B) The acausality of WEC control
The optimal WEC control problem has been well-framed and well-studied. By abstracting the WEC in the same structure as an electrical circuit (this can be done for any resonant device), Jacobi's maximum power transfer law gives a straightforward means of optimizing WEC power absorption. This is the so-called complex conjugate control, where a control law can be written explicitly as the complex conjugate of the WEC's intrinsic impedance. The only issue with this otherwise straightforward result is that the complex conjugate of the impedance is acausal. This, in fact, is quite true. However, when we consider the problem with an engineering perspective, and note that the energy in ocean waves almost entirely lies within a relatively narrow frequency band (periods of $5 < T < 15$ s), the situation improves. By considering the complex conjugate control problem over a finite bandwidth (which neglects only the small amounts of energy in surface ripples and tsunami waves at high and low frequencies, respectively), a causal controller can be defined such that it follows the frequency response of the complex conjugate controller as closely as possible. The only input to the controller is the device velocity. The most simplest causal controller may be a proportional-integral (PI) controller represented by a first-order transfer

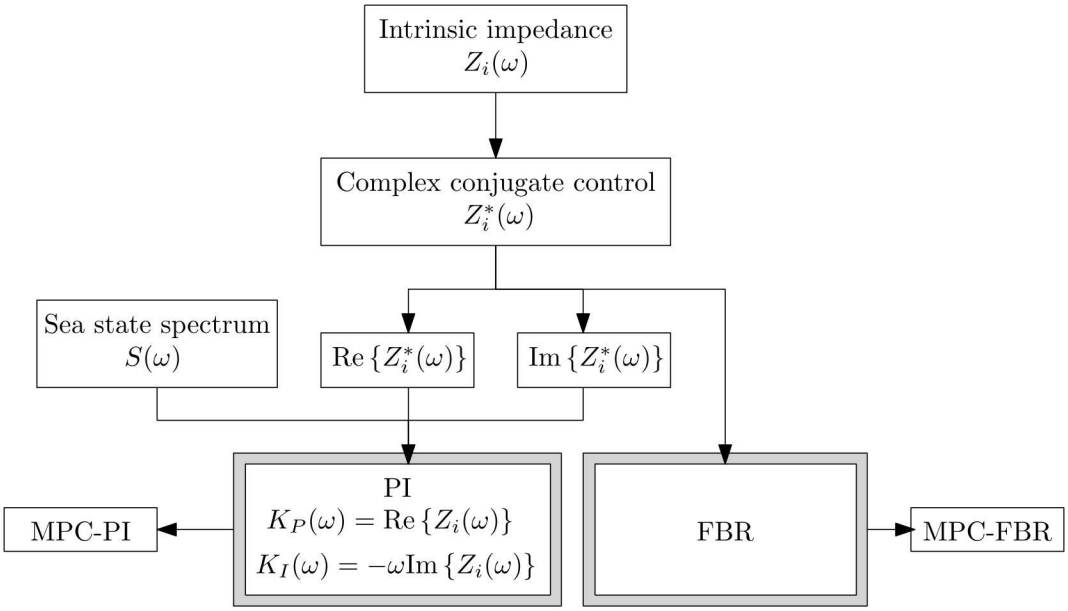

Figure 1.1: Hierarchy for WEC control design.

function. However, it matches the complex conjugate only locally, so using fitting techniques, such as system identification, a more optimal causal controller with higher order called the feedback resonating (FBR) controller is developed.

1.1 Introduction

Figure 1.1 shows a hierarchy of WEC control. The common starting point is the intrinsic impedance of the WEC, which can be obtained numerically or experimentally [2] (see Section 1.3 for further discussion). From the intrinsic impedance, we can formulate the so-called complex conjugate control, which is the optimal power transfer for a WEC (Section 1.3). PI and FBR controllers can be developed (Sections 1.4.1 and 1.4.2, respectively) as causal realizations of the complex conjugate control. The controllers can in turn be utilized by a model predictive controller (MPC) to allow for constraints (Section 1.5.2). Note that the MPC shown in Figure 1.1 is different from that typically considered for WEC control, in that it utilizes the knowledge of the intrinsic impedance to avoid the need for extended wave prediction. The more "classical" version of MPC, which requires prediction of incoming waves, is discussed in Section 1.5.1.

This report provides an in-depth explanation of each of these control strategies (Sections 1.3-1.5). Each of these controllers' performance is compared for a series of sea states (Chapter 2). For the "classical" MPC, various means of prediction, including a "perfect prediction" model are considered.

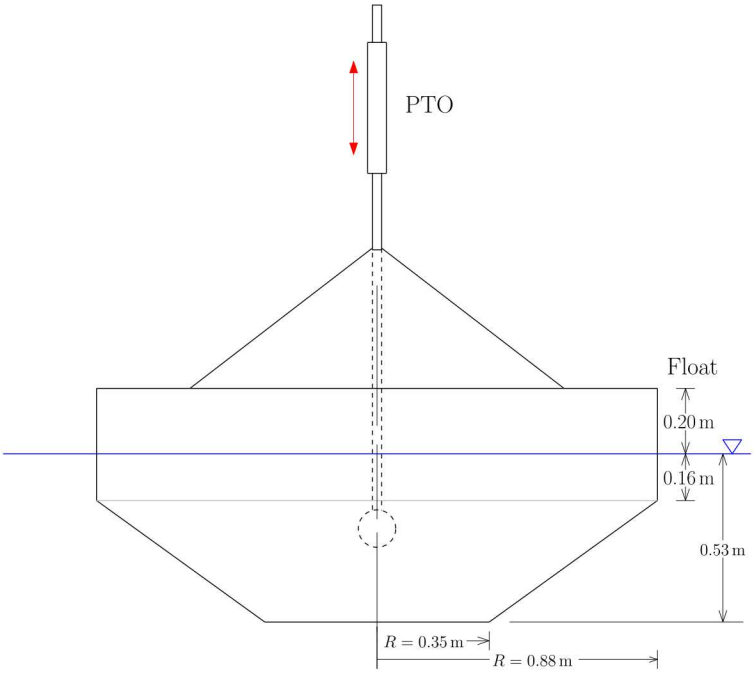

Figure 1.2: Study device diagram.

Table 1.1: Model-scale WEC physical parameters.

Parameter	Value
Rigid-body mass (float & slider), M [kg]	858
Displaced volume, $\forall$ [m^3]	0.858
Float radius, r [m]	0.88
Float draft, T [m]	0.53
Water density, ρ [kg/m^3]	1000
Water depth, h [m]	6.1
Linear hydrostatic stiffness, S [kN/m]	23.9
Infinite-frequency added mass, m_∞ [kg]	782
Max vertical travel, $\lvert z_{\max} \rvert$ [m]	0.6

1.2 Study device and sea states

A single degree of freedom heaving point absorber was selected for the case study discussed herein. This device has been studied previously for numerical control design [3, 4] and experimental testing [2, 5, 6]. Figure 1.2 and Table 1.1 show a diagram of the WEC device and its relevant physical parameters.

In this report, the incoming waves include ten different sea states, all of which are of JONSWAP type spectra and are summarized in Table 1.2. To assess performance, each controller has been analyzed numerically in these ten sea states.

Table 1.2: List of sea states inserted into the plant (WEC device).

Test Case	Peak period, T_p [s]	Significant wave height, H_s [in]	Peak enhancement factor, γ [-]
1	1.58	5	1
2	1.58	5	3.3
3	2.5	5	1
4	2.5	5	3.3
5	2.5	10	1
6	2.5	10	3.3
7	3.5	5	1
8	3.5	5	3.3
9	3.5	10	1
10	3.5	10	3.3

1.3 Complex conjugate control

The general structure (loss free) for energy transfer for the WEC device is that the incoming waves produce a force on the body, denoted as F_e, while the body radiates a wave back into the environment, denoted as F_{rad}. This formulation is based on linear potential flow theory (see, e.g., [7, 8]). The force on the WEC is then transferred onto the power take off (PTO), denoted as F_{pto}. In general, the equations of motion are defined as

$$[i\omega(M+m(\omega))+B_v+R(\omega)+\frac{S}{i\omega}]v(\omega)=F_e(\omega)+F_{pto}(\omega). \tag{1.1}$$

where ω is the angular velocity, M is the mass matrix of the device, $m(\omega)$ is the added mass, B_v is the damping, $R(\omega)$ is the radiation damping, S is the hydro-static restoring coefficient matrix, and $v(\omega)$ is the velocity of the buoy.

Now we will define the power absorption as

$$W_{pto}=-\frac{1}{2\pi}\int_0^\infty [F_{pto}(\omega)v^*(\omega)+F^*_{pto}(\omega)v(\omega)]d\omega, \tag{1.2}$$

where the asterisk (*) denotes the complex conjugate of a quantity. From the equation of motion defined in (1.1), the intrinsic impedance of the system is defined as

$$Z_i(\omega)=i\omega(M+m(\omega))+B_v+R(\omega)+\frac{S}{i\omega}. \tag{1.3}$$

From (1.3), we see that when the PTO force satisfies

$$F_{pto}(\omega)=-Z_i^*(\omega)v(\omega), \tag{1.4}$$

using (1.4) and determining the responses for $v^*(\omega)$, then (1.2) becomes

$$W_{pto,MAX}=\frac{1}{2\pi}\int_0^\infty \frac{|F_e(\omega)|^2}{2R_i(\omega)}d\omega, \tag{1.5}$$

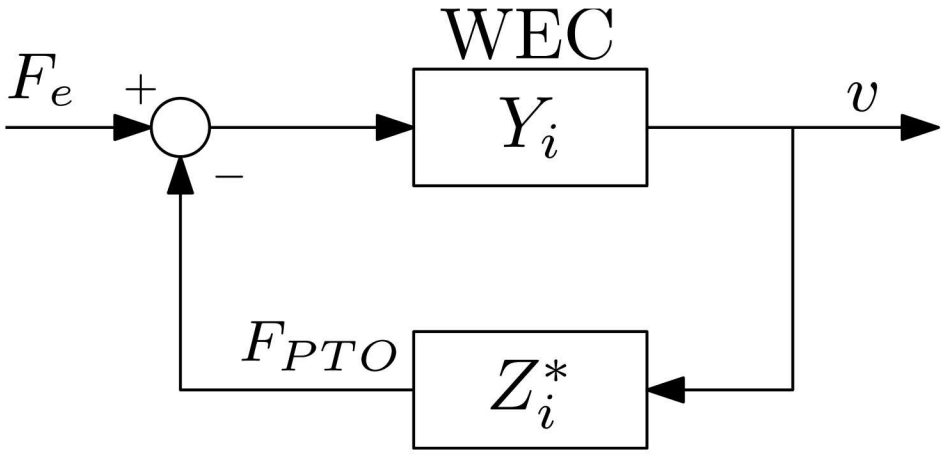

Figure 1.3: Controller model for reactive control for a WEC.

where $R_i(\omega)$ is the intrinsic resistance of the device which is equal to the real part of the intrinsic impedance ($\mathrm{Re}\{Z_i(\omega)\}$).

From this we can see that the optimal velocity corresponding to the maximum energy is $v(\omega) = \frac{F_e(\omega)}{2R_i(\omega)}$. From (1.4) we can see where the term complex conjugate control or impedance matching comes from. This basic feedback controller model can be shown in Figure 1.3, where Y_i is the intrinsic admittance of the device which is the inverse of the intrinsic impedance, i.e., $Y_i = 1/Z_i$. Maximum power absorption is achieved when the PTO impedance matches the complex conjugate of the mechanical impedance of the device, or when the reactance of the PTO cancels the reactance of the device. To see that the complex conjugate (CC) controller has a noncausal response we will look at the impulse response of the controller:

$$h_i(t) = W(t) + B_v\sqrt{2\pi}\delta(t) - M\sqrt{2\pi}\dot{\delta}(t) - S\sqrt{\frac{\pi}{2}}sgn(t). \tag{1.6}$$

Here, $W(t)$ is the causal impulse response of the radiation impedance, $\delta(t)$ and $\dot{\delta}(t)$ are the Dirac delta function and its time derivative respectively, and $sgn(t)$ is the sign function. We can see that the last term in (1.6) is the noncausal term where $h_i(t) = S\sqrt{\frac{\pi}{2}}$ for $t < 0$. Due to this noncausal response for the complex conjugate controller, the controller requires some future knowledge to be implemented. Hence, we will now explore methods that will have a causal realization of this controller, with the feedback control trying to closely match the complex conjugate of the mechanical impedance.

1.4 Causal realization

To determine a causal implementation of the complex conjugate feedback controller, we will use two general strategies, a PI controller and system identification (SID). For the PI controller, we determine the optimal P and I gains to be implemented for each individual wave spectrum. As can

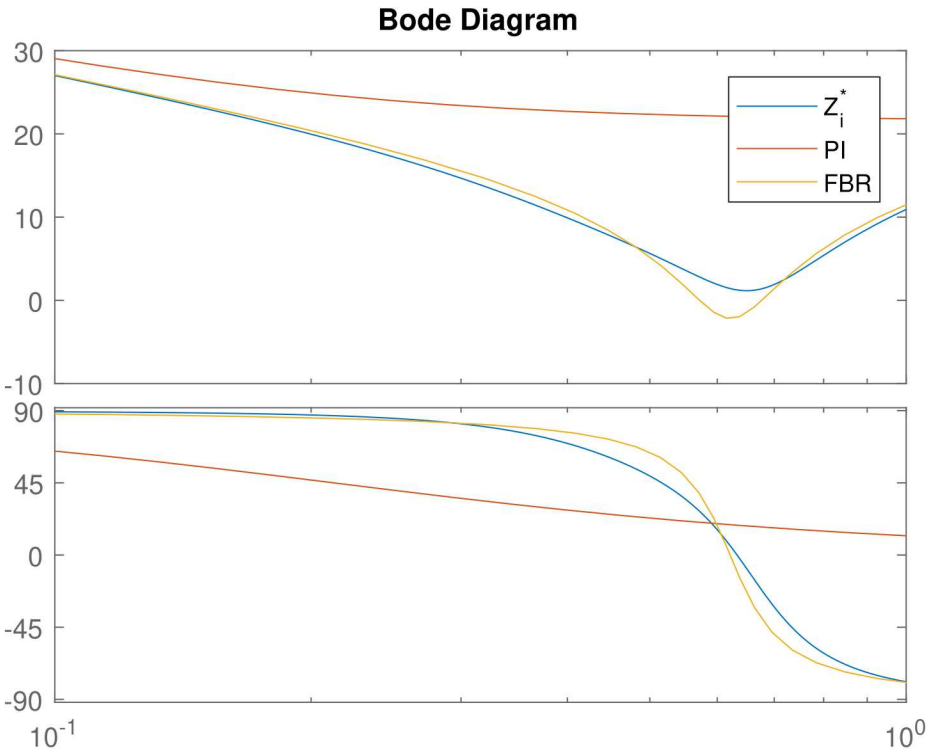

Figure 1.4: Bode diagram comparing the complex conjugate controller response (Z_i^*) with stable causal realizations for PI ($f_p = 0.6667$ Hz) and FBR controllers.

be seen in Figure 1.4 the PI controller will only match the complex conjugate at one point for the phase and magnitude response. In general the strategy is to match the PI controller as close to the complex conjugate as possible while still maintaining stability. As for the SID method, we will be using SID techniques to determine the best feedback controller response that matches the response of the complex conjugate, which lays the basis of the FBR controller. Again shown in Figure 1.4, we can see that the FBR, which is the SID matching for a second order system, better matches the complex conjugate response of the system.

1.4.1 PI control

The use of a PI controller allows to model the complex conjugate function as a first order system. In general we can model the feedback controller to have the following first order form,

$$U(s) = \frac{(K_P s + K_I)}{s} V(s), \tag{1.7}$$

where $U(s)$ and $V(s)$ are the Laplace transform of the control force $u(t)$ and the velocity of the buoy $v(t)$, respectively. Using (1.3), we can rewrite this equation to model that of a PI controller:

$$Z_i(s) = \frac{K_P s + K_I}{s}. \tag{1.8}$$

Table 1.3: Optimal I and P gains for each test case.

Test Case	K_I	K_P
1	-3221.91	2412.66
2	-1636.30	2255.87
3	-13748.70	2016.61
4	-13097.50	1946.55
5	-13786.30	2008.89
6	-13150.59	1939.29
7	-18510.49	1389.55
8	-18042.90	1345.76
9	-18566.14	1420.61
10	-18058.70	1340.85

With (1.8) and (1.3) we can determine the constant gains for the PI controller:

$$K_P(\omega) = \mathrm{Re}\{Z_i(\omega)\} = B_v + R(\omega) \tag{1.9}$$

and

$$K_I(\omega) = -\omega\,\mathrm{Im}\{Z_i(\omega)\} = -\omega^2(M + m(\omega)) + S. \tag{1.10}$$

As we can see determining (1.9) and (1.10) these values can only be determined at an individual frequency. As the frequency varies, the values of these gains will vary as well.

Due to this, it is expected for the PI controller to only be able to match the complex conjugate response in a small frequency band. As we have seen from the response in Figure 1.4 the PI controller matches the complex conjugate locally (around the designated frequency $f_p = 0.6667$ Hz) but the response error will grow larger outside of the frequency band. The optimal I and P gains that maximize the mean of mechanical power capture are specified in Table 1.3 for each test case listed in Table 1.2.

In this report, a simpler proportional (P) control is also considered for reference, which is often called the damping control. The damping control is pure P control with no I gain, i.e., $K_I = 0$ and this type of control has been frequently applied in the WEC control design, but is in general expected to have poorer performance than PI control. The optimal P gains are summarized in Table 1.4.

In order to improve the results of the power capture, SID techniques need to be used to determine more optimal higher order models to approximate a stable and causal response of the complex conjugate controller.

1.4.2 Feedback resonator

For a feedback resonator (FBR) controller, a causal implementation of the complex conjugate needs to be determined. The goal is to determine a feedback transfer function that can have a

Table 1.4: Optimal P gains for P (damping) control.

Test Case	K_P
1	2498.70
2	2267.88
3	4876.61
4	5022.55
5	4881.24
6	5030.47
7	8926.72
8	9342.90
9	8927.85
10	9347.21

stable causal response along with matching the magnitude and phase response of the complex conjugate, and SID techniques are needed to optimize this transfer function. For the purpose of this controller, the error in the phase for the SID model needs to be more minimized than the error in the magnitude.

SID methods are used in various engineering fields to produce models of various dynamic systems from measured data. SID techniques rely upon characterizing a system based on how the systems output responds to various inputs. Input signals are important as they effect the quality of output response, in other words if the dynamics of the system are not fully explored the SID model will not properly model the system. As such, the experiments used for the system identification have various advantages and disadvantages, such as signal bandwidth, improvement of model quality, cost of the experiment, and increased noise sensitivity.

SID techniques have been used to characterize WEC devices using various models and approaches [9]. The various model approaches can be characterized as white box (with model formulation), grey box (basic physical understanding of the system), and black box (no knowledge of the system). Typically for wave energy there is some knowledge of the system so SID techniques use grey box modeling.

With the built-in System Identification Toolbox in MATLAB, a greybox model can be used to determine the WEC's intrinsic impedance along with determining the complex conjugate model of the system. Since the complex conjugate is noncausal, the complex conjugate transfer function needs to be further modeled to determine a similar causal transfer function. To limit the model errors and increase likelihood of finding a causal model the SID needs to be applied over a specific frequency band. With a causal and stable model of the complex conjugate of the system a reactive controller can be built and implemented.

In Figure 1.4 the frequency band that we are specifically looking at is $0.1 - 1.0$ Hz. Using the built in SID methods within the MATLAB System Identification Toolbox we determine a new FBR model for each specific frequency band. Based on the similar magnitude and phase response

Table 1.5: FBR coefficients for each test case.

Test Case	a_1	a_0	b_2	b_1	b_0
1	85.05	0	-76.52	91.29	-1213
2	47.66	0	-40.56	53.64	-653.7
3	22.81	6.766	-17.73	26.26	-285.5
4	28.68	8.652	-22.44	34.6	-355.4
5	22.81	6.766	-17.73	26.26	-285.5
6	28.68	8.652	-22.44	34.6	-355.4
7	42.7	5.577	-36.27	46.43	-570.6
8	184.5	20.79	-162.1	214.9	-2471
9	42.7	5.577	-36.27	46.43	-570.6
10	184.5	20.79	-162.1	214.9	-2471

of the FBR to the complex conjugate response we expect to see the FBR controller to outperform the PI controller for all wave spectra.

In this report, the FBR controllers are obtained as transfer functions with two poles and two zeros in order to best match the complex conjugate. More specifically, every FBR transfer function is of the following form:

$$U(s) = \frac{b_2 s^2 + b_1 s + b_0}{s^2 + a_1 s + a_0} V(s). \tag{1.11}$$

The optimal coefficients in (1.11) for each test case are calculated such that the phase difference in the Bode diagram between the resulting FBR transfer function and the complex conjugate curve is minimized, which are listed in Table 1.5.

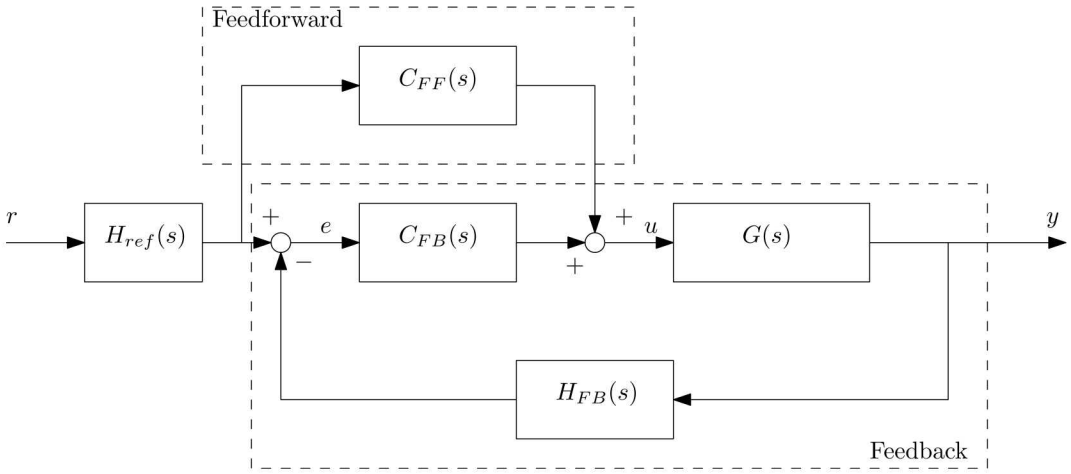

Figure 1.5: Basic feedforward (FF) + feedback (FB) controller structure [1].

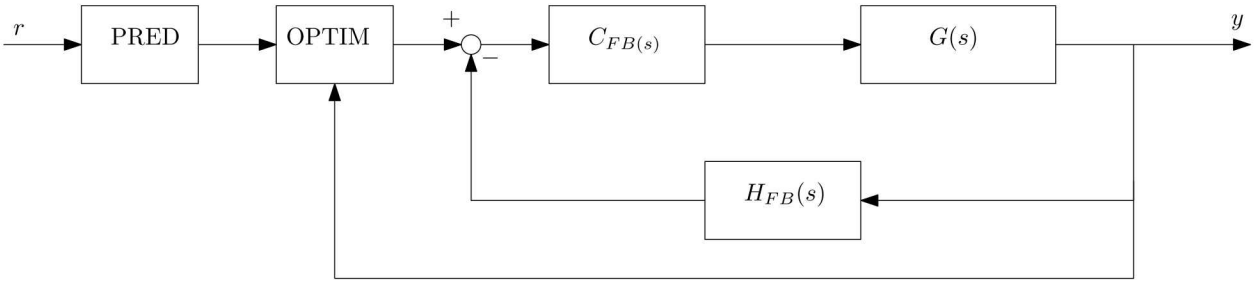

Figure 1.6: Basic structure for "receding horizon."

1.5 Model predictive control (MPC)

With an accurate WEC modeling via SID techniques, model predictive control (MPC) has many advantages over linear control strategies (i.e., PI or FBR) such as the capability to handle constraints and the optimization of a given cost function. However, it generally requires heavier computational loads due to prediction and optimization over a horizon and also it is more difficult to analyze the stability, robustness, and frequency-domain properties in the MPC design. In addition, the performance of an MPC can potentially depend upon the choice of a prediction method. Hence, in this section classical MPC is first introduced with the assumption of perfect prediction of a wave profile (Section 1.5.1). Next, a new MPC algorithm with a short prediction horizon (one time-step) is developed that is tuned via either a PI or an FBR feedback controller (Subsection 1.5.2). This new MPC will behave exactly as the predesigned PI or FBR controller when constraints are inactive that requires no prediction to bypass the acausality issue. It will also inherit "good" properties of linear control design and simultaneously be able to handle the constraints in an optimal manner when they are active. In the next section (Section 1.6), the classical MPC is again applied but with three different prediction methods since we do not have perfect knowledge of incoming wave profiles in real-life applications, and will be compared with the MPC with perfect prediction derived in Section 1.5.1.

1.5.1 Classical model predictive control

The general model predictive control (MPC) model is an optimization-based control strategy that is derived from attempting to solve a quadratic program (QP) in a receding horizon fashion (Figure 1.6). In this model, the inner feedback loop has not been considered, therefore the transfer function of the feedback block is $H_{FB}(s) = 0$ and the controller is $C_{FB}(s) = 1$, however as shown in Figure 1.6 the output, where y is the velocity of the buoy, of the system is passed to the optimization block directly. The signal r is the excitation force and the prediction block predicts the value of the excitation force over the prediction horizon, which is used by the optimizer to calculate the optimal motion and the corresponding force maximizing the absorbed power. The procedure is repeated periodically to compensate for disturbance and imperfect modeling by updating the current state of the system every time the optimization is carried out. For the "classical model" it is assumed in this section that perfect foreknowledge of the excitation is available. In general the wave model needs to be updated constantly, and in the next section (Section 1.6) the wave model is predicted via three different methods to construct MPC.

The derivation of the MPC control law begins with the specification of the WEC model used for control (controller model), which is the continuous-time state-space model [10]:

$$\begin{aligned} \dot{\boldsymbol{x}}_c(t) &= \mathbf{A}_c \boldsymbol{x}_c(t) + \mathbf{B}_c(u_c(t) + v_c(t)), \\ \boldsymbol{y}_c(t) &= \mathbf{C}_c \boldsymbol{x}_c(t), \end{aligned} \tag{1.12}$$

where $u_c(t)$ is the PTO force per unit mass and $v_c(t)$ is the excitation force per unit mass. Here, the state vector $\boldsymbol{x}_c$ and the output vector $\boldsymbol{y}_c$ are defined, respectively, as

$$\boldsymbol{x}_c = \begin{bmatrix} z \\ \dot{z} \\ \boldsymbol{x}_r \end{bmatrix} \in \mathbb{R}^{2+n}, \qquad \boldsymbol{y}_c = \begin{bmatrix} z \\ \dot{z} \end{bmatrix} \in \mathbb{R}^2, \tag{1.13}$$

where n is the order of the radiation subsystem model. The vertical position of the buoy is denoted by z and $\boldsymbol{x}_r \in \mathbb{R}^n$ is the state vector of radiation dynamics. The matrices $\mathbf{A}_c$, $\mathbf{B}_c$ and $\mathbf{C}_c$ are

$$\mathbf{A}_c = \begin{bmatrix} 0 & 1 & \mathbf{0} \\ \frac{-S}{M+m_\infty} & \frac{-B_v}{M+m_\infty} & \frac{-1}{M+m_\infty}\mathbf{C}_r \\ \mathbf{0} & \mathbf{B}_r & \mathbf{A}_r \end{bmatrix} \in \mathbb{R}^{(n+2)\times(n+2)}, \tag{1.14}$$

$$\mathbf{B}_c = \begin{bmatrix} 0 \\ 1 \\ \mathbf{0} \end{bmatrix} \in \mathbb{R}^{(n+2)\times 1}, \qquad \mathbf{C}_c = \begin{bmatrix} 1 & 0 & \mathbf{0} \\ 0 & 1 & \mathbf{0} \end{bmatrix} \in \mathbb{R}^{2\times(n+2)}, \tag{1.15}$$

where S is the hydrostatic restoring coefficient, B_v is a linear damping term describing the viscous effects of the fluid (and/or any other linear friction terms), M is the mass of the buoy and m_∞ is the asymptotic value of the added mass. In this report, the values $S = 23981.45$ N/m, $B_v = 380$ kg/s, and $M + m_\infty = 1640.02$ kg are employed. The matrices $\mathbf{A}_r$, $\mathbf{B}_r$ and $\mathbf{C}_r$, as usual, describe the dynamics of the radiation force (f_r):

$$\begin{aligned} \dot{\boldsymbol{x}}_r(t) &= \mathbf{A}_r \boldsymbol{x}_r(t) + \mathbf{B}_r \dot{z}(t), \\ f_r(t) &= \mathbf{C}_r \boldsymbol{x}_r, \end{aligned} \tag{1.16}$$

where

$$\mathbf{A}_r = \begin{bmatrix} -3.9913 & -2.6621 \\ 4 & 0 \end{bmatrix}, \mathbf{B}_r = \begin{bmatrix} 64 \\ 0 \end{bmatrix}, \mathbf{C}_r = \begin{bmatrix} 104.4457 & 0 \end{bmatrix}. \tag{1.17}$$

The MPC algorithm requires the dynamic model to be formulated in discrete time: following [10], the discretization of the model in (1.12) is carried out by means of a first order-hold, which results in continuous and piecewise linear profile for the optimal force. The benefit of this type of discretization is to allow for a longer update interval compared to a zero-hold discretization, which provides only a discontinuous, piecewise constant profile for the optimal control force. The state space model resulting from the discretization is:

$$\boldsymbol{x}(k+1) = \mathbf{A}\boldsymbol{x}(k) + \mathbf{B}\Delta u(k+1) + \mathbf{F}\Delta v(k+1), \tag{1.18}$$

$$\boldsymbol{y}(k) = \mathbf{C}\boldsymbol{x}(k), \tag{1.19}$$

where $\Delta u(k+1) = u_d(k+1) - u_d(k)$ and $\Delta v(k+1) = v_d(k+1) - v_d(k)$. Here, u_d and v_d denote the sampled versions of u_c and v_c, respectively, and

$$\mathbf{A} = \begin{bmatrix} \boldsymbol{\phi}(h) & \boldsymbol{\Gamma} & \boldsymbol{\Gamma} \\ \mathbf{0} & 1 & 0 \\ \mathbf{0} & 0 & 1 \end{bmatrix} \in \mathbb{R}^{(n+4)\times(n+4)}, \qquad \mathbf{B} = \begin{bmatrix} \boldsymbol{\Lambda} \\ 1 \\ 0 \end{bmatrix} \in \mathbb{R}^{(n+4)\times 1}, \tag{1.20}$$

$$\mathbf{F} = \begin{bmatrix} \boldsymbol{\Lambda} \\ 0 \\ 1 \end{bmatrix} \in \mathbb{R}^{(n+4)\times 1}, \qquad \mathbf{C} = \begin{bmatrix} 1 & 0 & 0 & \dots & 0 & 0 & 0 \\ 0 & 1 & 0 & \dots & 0 & 0 & 0 \\ 0 & 0 & 1 & \dots & 0 & 0 & 0 \end{bmatrix} \in \mathbb{R}^{3\times(n+4)}. \tag{1.21}$$

Here, $\boldsymbol{\phi}(h) = e^{\mathbf{A}_c h}$, where h is the update interval and

$$\boldsymbol{\Gamma} = \mathbf{A}_c^{-1}\left(\boldsymbol{\phi}(h) - \mathbf{I}\right)\mathbf{B}_c \ \in \mathbb{R}^{(n+2)\times 1}, \tag{1.22}$$

$$\boldsymbol{\Lambda} = \frac{1}{h}\mathbf{A}_c^{-1}\left(\boldsymbol{\Gamma} - h\mathbf{B}_c\right) \quad \in \mathbb{R}^{(n+2)\times 1}. \tag{1.23}$$

Let N denote the number of prediction steps, then the predicted output of the system can be written as a function of the current state and future input increments:

$$\underline{\boldsymbol{y}}(k) = \mathscr{P}\boldsymbol{x}(k) + \mathscr{T}_u\underline{\Delta\boldsymbol{u}}(k) + \mathscr{T}_v\underline{\Delta\boldsymbol{v}}(k), \tag{1.24}$$

where $\mathscr{P}$, $\mathscr{T}_u$ and $\mathscr{T}_v$ are

$$\mathscr{P} = \begin{bmatrix} \mathbf{CA} \\ \mathbf{CA}^2 \\ \vdots \\ \mathbf{CA}^N \end{bmatrix} \in \mathbb{R}^{3N\times(n+4)}, \tag{1.25}$$

$$\mathscr{T}_u = \begin{bmatrix} \mathbf{CB} & \mathbf{0} & \mathbf{0} & \dots \\ \mathbf{CAB} & \mathbf{CB} & \mathbf{0} & \dots \\ \mathbf{CA}^2\mathbf{B} & \mathbf{CAB} & \mathbf{CB} & \dots \\ \vdots & \vdots & \vdots & \vdots \\ \mathbf{CA}^{N-1}\mathbf{B} & \mathbf{CA}^{N-2}\mathbf{B} & \mathbf{CA}^{N-3}\mathbf{B} & \dots \end{bmatrix} \in \mathbb{R}^{3N\times N}, \tag{1.26}$$

$$\mathscr{T}_v = \begin{bmatrix} \mathbf{CF} & \mathbf{0} & \mathbf{0} & \dots \\ \mathbf{CAF} & \mathbf{CF} & \mathbf{0} & \dots \\ \mathbf{CA}^2\mathbf{F} & \mathbf{CAF} & \mathbf{CF} & \dots \\ \vdots & \vdots & \vdots & \vdots \\ \mathbf{CA}^{N-1}\mathbf{F} & \mathbf{CA}^{N-2}\mathbf{F} & \mathbf{CA}^{N-3}\mathbf{F} & \dots \end{bmatrix} \in \mathbb{R}^{3N\times N}. \tag{1.27}$$

The quantity to be maximized is the mechanical work done by the device over the prediction horizon T, expressed as:

$$E_{t,t+T} = -(M+m_\infty)\int_t^{t+T} u(\tau)\dot{z}(\tau)\,d\tau. \tag{1.28}$$

By means of the discretization, this quantity can be written in matrix form as the quadratic cost function J, defined as

$$J = \frac{1}{2}\underline{\Delta \boldsymbol{u}}'\,\mathscr{T}_u'\underline{\mathbf{Q}}\,\mathscr{T}_u\underline{\Delta \boldsymbol{u}} + \underline{\Delta \boldsymbol{u}}'\,\mathscr{T}_u'\underline{\mathbf{Q}}\,(\mathscr{P}\boldsymbol{x} + \mathscr{T}_v\underline{\Delta \boldsymbol{v}}), \tag{1.29}$$

where $\underline{\mathbf{Q}}$ is:

$$\underline{\mathbf{Q}} = \begin{bmatrix} \underline{\mathbf{M}} & & & \\ & \ddots & & \\ & & \underline{\mathbf{M}} & \\ & & & \frac{1}{2}\underline{\mathbf{M}} \end{bmatrix}, \qquad \underline{\mathbf{M}} = \begin{bmatrix} 0 & 0 & 0 \\ 0 & 0 & 1 \\ 0 & 1 & 0 \end{bmatrix}. \tag{1.30}$$

Constraints on the maximum force and maximum displacement can be included in the formulation of the optimization problem using the linear inequalities

$$\begin{bmatrix} \mathbf{M}_z \\ -\mathbf{M}_z \end{bmatrix} \mathscr{T}_u\underline{\Delta \boldsymbol{u}} \;\leq\; \begin{bmatrix} -\mathbf{M}_z \\ \mathbf{M}_z \end{bmatrix} (\mathscr{P}\boldsymbol{x} + \mathscr{T}_v\underline{\Delta \boldsymbol{v}}) + z_{max}, \tag{1.31}$$

$$\begin{bmatrix} \mathbf{M}_f \\ -\mathbf{M}_f \end{bmatrix} \mathscr{T}_u\underline{\Delta \boldsymbol{u}} \;\leq\; \begin{bmatrix} -\mathbf{M}_f \\ \mathbf{M}_f \end{bmatrix} (\mathscr{P}\boldsymbol{x} + \mathscr{T}_v\underline{\Delta \boldsymbol{v}}) + f_{max}, \tag{1.32}$$

where $\mathbf{M}_z$ and $\mathbf{M}_f$ are

$$\mathbf{M}_z = \begin{bmatrix} \mathbf{C}_z & & & \\ & \ddots & & \\ & & \mathbf{C}_z & \\ & & & \mathbf{C}_z \end{bmatrix} \in \mathbb{R}^{N\times 3N}, \quad \mathbf{C}_z = [1\,0\,0], \tag{1.33}$$

$$\mathbf{M}_f = \begin{bmatrix} \mathbf{C}_f & & & \\ & \ddots & & \\ & & \mathbf{C}_f & \\ & & & \mathbf{C}_f \end{bmatrix} \in \mathbb{R}^{N\times 3N}, \quad \mathbf{C}_f = [0\,0\,1]. \tag{1.34}$$

1.5.2 MPC that behaves as a PI or FBR controller

In this section, a new tuning method for MPC weight matrices using a feedback controller (either PI or FBR) is introduced. It is shown that any linear controller in a state feedback or a proper rational transfer function form can be realized via MPC with specially tuned weight matrices. Since a PI or an FBR controller developed in the previous section 1.4 is a simple example of state feedback control, we can easily apply this method to obtain MPC that exactly behaves as the predesigned PI or FBR controller "with no prediction" when constraints are not active, thereby avoiding the acausality problem. Of course, the MPC can still optimally deal with active constraints, which clearly distinguishes the PI or the FBR controller. In this section, the MPC is created for unconstrained cases; constrained cases are investigated in Appendix A where the control input saturation is considered as the constraint.

The MPC signals are computed by the Model Predictive Control Toolbox of MATLAB in this section, while in the previous Section 1.5.1, they were obtained by the algorithms proposed in [10] based on the custom cost function (1.29) for a WEC system. At every control cycle $k = 0, 1, ...$, the MPC Toolbox solves the following finite-horizon optimal control problem:

$$\mathscr{V}(\boldsymbol{x}(k), \boldsymbol{u}(k)) = \min_{\boldsymbol{U}(k)} \boldsymbol{x}'(N|k)\mathbf{P}\boldsymbol{x}(N|k) + \sum_{i=0}^{N-1} \boldsymbol{x}'(i|k)\mathbf{Q}\boldsymbol{x}(i|k) + \boldsymbol{u}'(i|k)\mathbf{R}\boldsymbol{u}(i|k) \tag{1.35}$$

s.t.

$$\boldsymbol{x}(i+1|k) = \mathbf{A}\boldsymbol{x}(i|k) + \mathbf{B}\boldsymbol{u}(i|k), \quad i = 0, ..., N-1, \tag{1.36}$$

$$x_{min} \leq \|\boldsymbol{x}(i|k)\| \leq x_{max}, \quad i = 0, ..., N, \tag{1.37}$$

$$u_{min} \leq \|\boldsymbol{u}(i|k)\| \leq u_{max}, \quad i = 0, ..., N-1, \tag{1.38}$$

$$\boldsymbol{x}(0|k) = \boldsymbol{x}(k), \tag{1.39}$$

where (1.36) is the discrete-time state space equation of the plant model, $\boldsymbol{x} \in \mathbb{R}^n$ is the state vector, $\boldsymbol{u} \in \mathbb{R}^m$ is the control input vector, N is the prediction horizon, $\boldsymbol{U}(k) = [\boldsymbol{u}'(0|k) \ ... \ \boldsymbol{u}'(N-1|k)] \in \mathbb{R}^{Nm}$ is the vector to be optimized, and $\mathscr{V} : \mathbb{R}^n \to \mathbb{R}_{0+}$ is the value function. The matrices $\mathbf{P} \in \mathbb{R}^{n \times n}$, $\mathbf{Q} \in \mathbb{R}^{n \times n}$, and $\mathbf{R} \in \mathbb{R}^{m \times m}$ are the weight matrices that shall be tuned shortly.

Assuming that the current state $\boldsymbol{x}(k)$ is given, the finite horizon optimal control problem (1.35) can be reformulated to the following QP with respect to $\boldsymbol{U}(k)$

$$\min_{\boldsymbol{U}(k)} \boldsymbol{U}'(k)\mathbf{H}\boldsymbol{U}(k) + 2\boldsymbol{x}'(k)\mathbf{F}\boldsymbol{U}(k) \tag{1.40}$$

s.t.

$$\mathbf{G}\boldsymbol{U}(k) \leq \boldsymbol{\lambda} + \boldsymbol{\Lambda}\boldsymbol{x}(k), \tag{1.41}$$

where $\mathbf{G} \in \mathbb{R}^{q \times Nm}$, $\boldsymbol{\lambda} \in \mathbb{R}^q$, and $\boldsymbol{\Lambda} \in \mathbb{R}^{q \times n}$ are the problem constraints. Also, the following new matrices are defined in (1.40)

$$\mathbf{H} = \mathscr{R} + \mathscr{S}'\mathscr{Q}\mathscr{S}, \ \ \mathbf{F} = \mathscr{T}'\mathscr{Q}\mathscr{S}, \tag{1.42}$$

where $\mathscr{S}$ is the N-steps state reachability matrix, $\mathscr{T}$ is the N-steps free evolution matrix

$$\mathscr{S} = \begin{bmatrix} \mathbf{B} & \mathbf{0} & \dots & \mathbf{0} \\ \mathbf{AB} & \mathbf{B} & \dots & \mathbf{0} \\ \vdots & \vdots & \ddots & \vdots \\ \mathbf{A}^{N-1}\mathbf{B} & \mathbf{A}^{N-2}\mathbf{B} & \dots & \mathbf{B} \end{bmatrix}, \quad \mathscr{T} = \begin{bmatrix} \mathbf{A} \\ \mathbf{A}^2 \\ \vdots \\ \mathbf{A}^N, \end{bmatrix}, \tag{1.43}$$

and $\mathscr{Q} \in \mathbb{R}^{Nn \times Nn}$, $\mathscr{R} \in \mathbb{R}^{Nm \times Nm}$ are block-diagonal matrices

$$\mathscr{Q} = \begin{bmatrix} \mathbf{Q} & \mathbf{0} & \mathbf{0} & \dots & \mathbf{0} \\ \mathbf{0} & \mathbf{Q} & \mathbf{0} & \dots & \mathbf{0} \\ \vdots & \vdots & \ddots & \vdots & \vdots \\ \mathbf{0} & \mathbf{0} & \dots & \mathbf{Q} & \mathbf{0} \\ \mathbf{0} & \mathbf{0} & \dots & \mathbf{0} & \mathbf{P} \end{bmatrix}, \quad \mathscr{R} = \begin{bmatrix} \mathbf{R} & \mathbf{0} & \dots & \mathbf{0} \\ \mathbf{0} & \mathbf{R} & \dots & \mathbf{0} \\ \vdots & \vdots & \ddots & \vdots \\ \mathbf{0} & \dots & \mathbf{0} & \mathbf{R} \end{bmatrix}. \tag{1.44}$$

When constraints are not active, the QP (1.40) has the unconstrained optimal solution $\boldsymbol{U}^*(k)$ which is given by

$$\boldsymbol{U}^*(k) = \begin{bmatrix} \boldsymbol{u}^*(0|k) \\ \vdots \\ \boldsymbol{u}^*(N-1|k) \end{bmatrix} = -\mathbf{H}^{-1}\mathbf{F}'\boldsymbol{x}(k). \tag{1.45}$$

The MPC command at step k then picks up only the first move such that

$$\boldsymbol{u}_{\mathrm{MPC}}(\boldsymbol{x}(k)) = \boldsymbol{u}^*(0|k) = -\boldsymbol{\Gamma}\mathbf{H}^{-1}\mathbf{F}'\boldsymbol{x}(k), \tag{1.46}$$

where $\boldsymbol{\Gamma} = [\mathbf{I}_m \ \ \mathbf{0} \ \ \dots \ \ \mathbf{0}]$.

Now, we consider a predesigned linear controller in a state feedback form

$$\boldsymbol{u}_{\mathrm{LN}}(k) = \mathbf{K}\boldsymbol{x}(k), \ \ \mathbf{K} \in \mathbb{R}^{m \times n}. \tag{1.47}$$

Then, the objective is to find weight matrices $\mathbf{P}$, $\mathbf{Q}$, and $\mathbf{R}$ in (1.35) such that

$$-\boldsymbol{\Gamma}\mathbf{H}^{-1}\mathbf{F}' = \mathbf{K}, \tag{1.48}$$

where $\mathbf{K}$ is given.

In brief, once the weight matrices $\mathbf{P}$, $\mathbf{Q}$, and $\mathbf{R}$ are found that satisfy (1.48) given $\mathbf{K}$, then the MPC with the cost function (1.35) behaves as the linear controller of the form (1.47), when the constraints are not active. Di Cairano and Bemporad [11] presented approximate solutions for the weight matrices $\mathbf{Q}$, $\mathbf{R}$, and $\mathbf{P}$ by recasting (1.48) as a convex optimization problem with linear matrix inequalities constraints. In most cases these solutions provide pretty accurate results, however, they necessitate a numerical optimization solver and the performance can potentially deteriorate due to the intentionally added constraints to make the problem convex. Hence, we now propose new analytical solutions that immediately calculate $\mathbf{Q}$, $\mathbf{R}$, and $\mathbf{P}$ by directly solving (1.48). We consider here the case $N = 2$ because shorter horizon requires less computational loads and the control performance is independent of N in an unconstrained application. On the other

hand, when constraints are active, a short horizon might degrade the control performance due to inaccurate prediction. However, in this report, even for constrained cases, the prediction horizon $N = 2$ is applied because good performance is still observed as shown in Appendix A. Use of longer prediction horizon will be handled in future work.

When $N = 2$, the matrices $\mathscr{S}$, $\mathscr{T}$, $\mathscr{Q}$, and $\mathscr{R}$ in (1.43) and (1.44) are simplified as

$$\mathscr{S} = \begin{bmatrix} \mathbf{B} & \mathbf{0} \\ \mathbf{AB} & \mathbf{B} \end{bmatrix}, \quad \mathscr{T} = \begin{bmatrix} \mathbf{A} \\ \mathbf{A}^2 \end{bmatrix}, \quad \mathscr{Q} = \begin{bmatrix} \mathbf{Q} & \mathbf{0} \\ \mathbf{0} & \mathbf{P} \end{bmatrix}, \quad \mathscr{R} = \begin{bmatrix} \mathbf{R} & \mathbf{0} \\ \mathbf{0} & \mathbf{R} \end{bmatrix}. \tag{1.49}$$

Here, $\mathbf{R}$ is a scalar if a single control input (i.e., $m = 1$) is considered. Accordingly, the matrices $\mathbf{H}$ and $\mathbf{F}'$ in (1.42) become

$$\mathbf{H} = \begin{bmatrix} \mathbf{R} + \mathbf{B}'\mathbf{Q}\mathbf{B} + \mathbf{B}'\mathbf{A}'\mathbf{P}\mathbf{A}\mathbf{B} & \mathbf{B}'\mathbf{A}'\mathbf{P}\mathbf{B} \\ \mathbf{B}'\mathbf{P}\mathbf{A}\mathbf{B} & \mathbf{R} + \mathbf{B}'\mathbf{P}\mathbf{B} \end{bmatrix}, \quad \mathbf{F}' = \begin{bmatrix} \mathbf{B}'\mathbf{Q}\mathbf{A} + \mathbf{B}'\mathbf{A}'\mathbf{P}\mathbf{A}^2 \\ \mathbf{B}'\mathbf{P}\mathbf{A}^2 \end{bmatrix}. \tag{1.50}$$

Then, the inverse of the 2 by 2 matrix $\mathbf{H}$ is directly calculated as

$$\mathbf{H}^{-1} = \frac{1}{\mathbf{D}} \begin{bmatrix} \mathbf{R} + \mathbf{B}'\mathbf{P}\mathbf{B} & -\mathbf{B}'\mathbf{A}'\mathbf{P}\mathbf{B} \\ -\mathbf{B}'\mathbf{P}\mathbf{A}\mathbf{B} & \mathbf{R} + \mathbf{B}'\mathbf{Q}\mathbf{B} + \mathbf{B}'\mathbf{A}'\mathbf{P}\mathbf{A}\mathbf{B} \end{bmatrix}, \tag{1.51}$$

where the determinant $\mathbf{D}$ is given by

$$\mathbf{D} = (\mathbf{R} + \mathbf{B}'\mathbf{Q}\mathbf{B} + \mathbf{B}'\mathbf{A}'\mathbf{P}\mathbf{A}\mathbf{B})(\mathbf{R} + \mathbf{B}'\mathbf{P}\mathbf{B}) - \mathbf{B}'\mathbf{A}'\mathbf{P}\mathbf{B}\mathbf{B}'\mathbf{P}\mathbf{A}\mathbf{B}. \tag{1.52}$$

When $m = 1$, we have $\mathbf{\Gamma} = [1 \;\; 0]$ in (1.46) and should find the matrices $\mathbf{Q}$, $\mathbf{R}$, and $\mathbf{P}$ for given $\mathbf{A}$, $\mathbf{B}$, and $\mathbf{K}$ that satisfy the following equation:

$$-\mathbf{\Gamma}\mathbf{H}^{-1}\mathbf{F}' = -\frac{1}{\mathbf{D}}[(\mathbf{R} + \mathbf{B}'\mathbf{P}\mathbf{B})(\mathbf{B}'\mathbf{Q}\mathbf{A} + \mathbf{B}'\mathbf{A}'\mathbf{P}\mathbf{A}^2) - \mathbf{B}'\mathbf{A}'\mathbf{P}\mathbf{B}\mathbf{B}'\mathbf{P}\mathbf{A}^2] = \mathbf{K}. \tag{1.53}$$

As shall be shown later, an FBR controller can be thought of as a variation of a Proportional, Integral, Derivative (PID) controller and a PI controller is of course a special case of a PID controller. Hence, consider the following 1 by 3 gain matrix $\mathbf{K}$:

$$\mathbf{K} = [K_I \;\; K_P \;\; K_D]. \tag{1.54}$$

Then, since any matrices $\mathbf{Q}$, $\mathbf{R}$, and $\mathbf{P}$ satisfying (1.53) can be solutions, let us first simplify (1.53) by choosing $\mathbf{P}$ such that $\mathbf{B}'\mathbf{P} = \mathbf{0}$. General solutions to $\mathbf{B}'\mathbf{P} = \mathbf{0}$ are given by

$$\mathbf{P} = (\mathbf{I} - (\mathbf{B}')^{+}\mathbf{B}')\mathbf{\Xi}, \tag{1.55}$$

where $(\mathbf{B}')^{+}$ is the Moore-Penrose generalized inverse of $\mathbf{B}'$ and $\mathbf{\Xi}$ is an arbitrary 3 by 3 matrix. However, for the use of MPC formulation, $\mathbf{P}$ must be positive definite to allow its Cholesky decomposition (see the User's Guide Manual of the MPC Toolbox for more details) so we select the matrix $\mathbf{\Xi}$ as $\mathbf{\Xi} = \zeta(\mathbf{I} - (\mathbf{B}')^{+}\mathbf{B}')$ with a positive constant ζ such that

$$\mathbf{P} = \zeta(\mathbf{I} - (\mathbf{B}')^{+}\mathbf{B}')^2. \tag{1.56}$$

Although (1.56) provides an exact solution to $\mathbf{B}'\mathbf{P} = \mathbf{0}$, the matrix $(\mathbf{I} - (\mathbf{B}')^{+}\mathbf{B}')$ is always rank deficient and $\mathbf{P}$ in (1.56) is always positive semi-definite, not positive definite. It is this reason that one additional term is added to (1.56):

$$\mathbf{P} = \zeta(\mathbf{I} - (\mathbf{B}')^{+}\mathbf{B}')^2 + \rho\mathbf{I}, \tag{1.57}$$

where ρ is a small positive number such that $\mathbf{B}'\mathbf{P}$ is sufficiently close to the zero matrix.

Once the matrix $\mathbf{P}$ is obtained by (1.57), $\mathbf{B}'\mathbf{P} = \mathbf{0}$ (approximately) holds and the determinant $\mathbf{D}$ becomes

$$\mathbf{D} = \mathbf{R}(\mathbf{R} + \mathbf{B}'\mathbf{Q}\mathbf{B} + \mathbf{B}'\mathbf{A}'\mathbf{P}\mathbf{A}\mathbf{B}). \tag{1.58}$$

Then, the main equation (1.53) to be solved for $\mathbf{Q}$ and $\mathbf{R}$ is simplified as

$$\mathbf{R}\mathbf{K} + \mathbf{B}'\mathbf{Q}\mathbf{\Phi} + \mathbf{\Psi} = \mathbf{0}, \tag{1.59}$$

where $\mathbf{\Phi} := \mathbf{A} + \mathbf{B}\mathbf{K}$ and $\mathbf{\Psi} := \mathbf{B}'\mathbf{A}'\mathbf{P}\mathbf{A}(\mathbf{A} + \mathbf{B}\mathbf{K})$. For the sake of simplicity, let us assume $\mathbf{Q}$ to be diagonal and decompose each matrix as

$$\mathbf{Q} = \begin{bmatrix} Q_1 & 0 & 0 \\ 0 & Q_2 & 0 \\ 0 & 0 & Q_3 \end{bmatrix}, \ \mathbf{K} = [K_I \ K_P \ K_D], \ \mathbf{B} = \begin{bmatrix} B_1 \\ B_2 \\ B_3 \end{bmatrix}, \ \mathbf{\Phi} = \begin{bmatrix} \Phi_{11} & \Phi_{12} & \Phi_{13} \\ \Phi_{21} & \Phi_{22} & \Phi_{23} \\ \Phi_{31} & \Phi_{32} & \Phi_{33} \end{bmatrix}, \ \mathbf{\Psi} = [\Psi_1 \ \Psi_2 \ \Psi_3], \tag{1.60}$$

and R is a scalar because only one control input is considered in this report. Substituting (1.60) into (1.59) yields the following equation:

$$\begin{bmatrix} K_I & B_1\Phi_{11} & B_2\Phi_{21} & B_3\Phi_{31} \\ K_P & B_1\Phi_{12} & B_2\Phi_{22} & B_3\Phi_{32} \\ K_D & B_1\Phi_{13} & B_2\Phi_{23} & B_3\Phi_{33} \end{bmatrix} \begin{bmatrix} R \\ Q_1 \\ Q_2 \\ Q_3 \end{bmatrix} = - \begin{bmatrix} \Psi_1 \\ \Psi_2 \\ \Psi_3 \end{bmatrix}. \tag{1.61}$$

There are four unknowns (R, Q_1, Q_2, Q_3) and three equations, and hence, there exist infinite number of solutions. For brevity, let us assume $Q_3 = \eta Q_2$ with some constant η and (1.61) becomes

$$\begin{bmatrix} K_I & B_1\Phi_{11} & B_2\Phi_{21} + \eta B_3\Phi_{31} \\ K_P & B_1\Phi_{12} & B_2\Phi_{22} + \eta B_3\Phi_{32} \\ K_D & B_1\Phi_{13} & B_2\Phi_{23} + \eta B_3\Phi_{33} \end{bmatrix} \begin{bmatrix} R \\ Q_1 \\ Q_2 \end{bmatrix} = - \begin{bmatrix} \Psi_1 \\ \Psi_2 \\ \Psi_3 \end{bmatrix}. \tag{1.62}$$

Then, the solution to (1.62) is easily found as

$$\begin{bmatrix} R \\ Q_1 \\ Q_2 \end{bmatrix} = - \begin{bmatrix} K_I & B_1\Phi_{11} & B_2\Phi_{21} + \eta B_3\Phi_{31} \\ K_P & B_1\Phi_{12} & B_2\Phi_{22} + \eta B_3\Phi_{32} \\ K_D & B_1\Phi_{13} & B_2\Phi_{23} + \eta B_3\Phi_{33} \end{bmatrix}^{-1} \begin{bmatrix} \Psi_1 \\ \Psi_2 \\ \Psi_3 \end{bmatrix}, \tag{1.63}$$

where it is assumed that the inverse matrix in (1.63) exists with a proper selection of η, and $Q_3 = \eta Q_2$. Hence, we have obtained the explicit solutions for $\mathbf{P}$, $\mathbf{Q}$, and $\mathbf{R}$ that are given in (1.57) and (1.63), respectively.

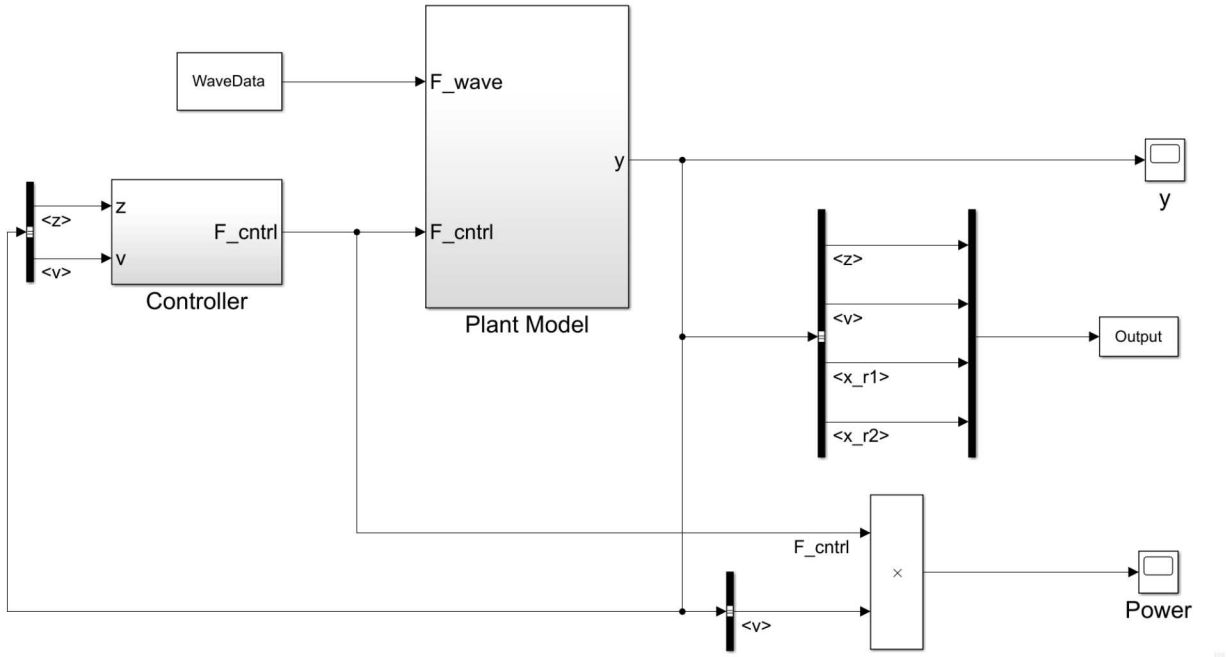

Figure 1.7: Block diagram of the controlled system.

Following the same procedure, we can derive the explicit solutions for a PI control case where $\mathbf{K} = [K_I \;\; K_P]$:

$$\begin{bmatrix} R \\ Q_1 \end{bmatrix} = -\begin{bmatrix} K_I & B_1\Phi_{11} + \eta B_2\Phi_{21} \\ K_P & B_1\Phi_{12} + \eta B_2\Phi_{22} \end{bmatrix}^{-1} \begin{bmatrix} \Psi_1 \\ \Psi_2 \end{bmatrix}, \tag{1.64}$$

where $Q_2 = \eta Q_1$ and the matrix $\mathbf{P}$ is again given by (1.57). In this case, R is a scalar and $\mathbf{Q}$ and $\mathbf{P}$ are 2 by 2 matrices.

The block diagram describing the controlled system is displayed in Figure 1.7. The control force signal is generated by the MPC and inserted into the WEC plant that is also disturbed by the wave force. Then, the plant outputs four signals (see the Cretel's model (1.12)), and among them the controller uses z and v (vertical position and velocity of the buoy, respectively) to calculate its control signal that is applied to the plant. The goal is to maximize the mechanical power capture which is the product of the control force and the velocity of the buoy.

Let us first design the MPC that behaves as a PI controller, so-called the MPC-PI, when constraints are inactive. Since only two state variables (z and v) are used for the MPC, a simplified plant model of a second order is employed in this report that is obtained by the MATLAB command `tfest`, instead of the fourth-order Cretel's model (1.12). In the simplified model, the input is the control signal and the outputs are z and v. The state-space representation in a controllable canonical form is given by

$$\begin{aligned} \dot{\boldsymbol{x}}(t) &= \mathbf{A}_c\boldsymbol{x}(t) + \mathbf{B}_c\boldsymbol{u}(t), \\ \boldsymbol{y}(t) &= \mathbf{C}_c\boldsymbol{x}(t) + \mathbf{D}_c\boldsymbol{u}(t), \end{aligned} \tag{1.65}$$

where $\boldsymbol{x}(t) = [z(t)\ v(t)]'$ is the state vector and $\boldsymbol{u}(t)$ is the control vector. The matrices in (1.65) are obtained by

$$\mathbf{A}_c = \begin{bmatrix} 0 & 1 \\ -15.66 & -1.369 \end{bmatrix},\ \mathbf{B}_c = \begin{bmatrix} 1.201 \\ -1.645 \end{bmatrix},\ \mathbf{C}_c = \begin{bmatrix} 1 & 0 \\ 0 & 1 \end{bmatrix},\ \mathbf{D}_c = \begin{bmatrix} 0 \\ 0 \end{bmatrix}. \tag{1.66}$$

Since an MPC needs a difference equation model, (1.65) must be transformed to a discrete-time representation:

$$\begin{aligned} \boldsymbol{x}(k+1) &= \mathbf{A}\boldsymbol{x}(k) + \mathbf{B}\boldsymbol{u}(k), \\ \boldsymbol{y}(k) &= \mathbf{C}\boldsymbol{x}(k) + \mathbf{D}\boldsymbol{u}(k), \end{aligned} \tag{1.67}$$

where $\cdot(k)$ is a quantity at the time step k and $\boldsymbol{x}(k) = [z(k)\ v(k)]'$. Assuming the sampling interval $T_s = 0.005$ s, the matrices in (1.67) are given by

$$\mathbf{A} = \begin{bmatrix} 0.9998 & 0.004983 \\ -0.07804 & 0.993 \end{bmatrix},\ \mathbf{B} = \begin{bmatrix} 0.005986 \\ -0.008431 \end{bmatrix},\ \mathbf{C} = \begin{bmatrix} 1 & 0 \\ 0 & 1 \end{bmatrix},\ \mathbf{D} = \begin{bmatrix} 0 \\ 0 \end{bmatrix}. \tag{1.68}$$

In discretizing (1.65), the zero-order hold method was employed to realize $\mathbf{D} = [0\ 0]'$ in (1.68) because the MPC Toolbox prohibits direct feedthrough from an input (i.e., manipulated variable) to an output.

Figure 1.8 shows the Bode diagram from the input $u(t)$ (control signal) to the output $v(t)$ obtained by the simplified model (1.65) and the original model (1.12) which has four state variables. From the Figure 1.8, it is found that the simplified model matches well the original one for the frequency range of interest ($f \in [0.1\ 1.0]$).

Then, a PI controller is easily designed in a form of (1.47) such that

$$\boldsymbol{u}_{\mathrm{PI}}(t) = \mathbf{K}\boldsymbol{x}(t), \tag{1.69}$$

where $\mathbf{K} = [K_I\ \ K_P]$ and K_I and K_P are the I and P gains respectively, shown in Table 1.3. Next, given the gain matrix $\mathbf{K}$, the weight matrices $\mathbf{P}$, $\mathbf{Q}$, and $\mathbf{R}$ used in the cost function of MPC are explicitly obtained by (1.57) and (1.64). In this report, the prediction horizon $N = 2$ is employed and the control horizon is set as the same as the prediction horizon N. The obtained control results such as the control forces, velocities of the buoy, and the mean power capture will be shown in Chapter 2.

Next, let us consider the MPC that behaves as an FBR controller (MPC-FBR), which can be developed in a similar manner. However, the FBR controllers are in a transfer function form, so we have to transform them to the state feedback form (1.47). In the time domain, (1.11) transforms to the following integro-differential equation:

$$\dot{u} + a_1 u + a_0 \int u dt = b_2 \dot{v} + b_1 v + b_0 z, \tag{1.70}$$

where zero initial conditions are assumed. Upon defining the left hand side of (1.70) as $U_c(t)$, (1.70) is rewritten as

$$U_c = [b_0\ \ b_1\ \ b_2] \begin{bmatrix} z \\ v \\ \dot{v} \end{bmatrix}. \tag{1.71}$$

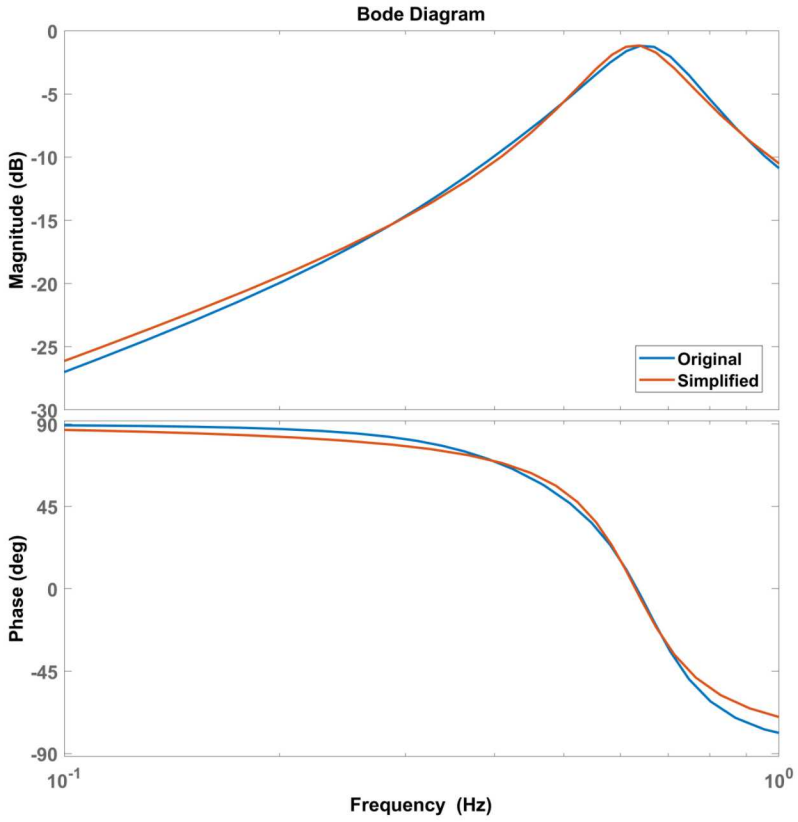

Figure 1.8: Bode diagram of the simplified (second order) and original (fourth order) models.

If the term $\dot{v}$ can be accurately evaluated via a numerical differentiator, (1.71) is exactly of the form of (1.47). Then, the actual control force $u(t)$ is retrieved by solving the integro-differential equation (1.70). Since (1.71) is exactly in the form of PID controllers, b_0, b_1, and b_2 correspond to K_I, K_P, and K_D, respectively. Once these gains are given as in Table 1.5, the weight matrices $\mathbf{P}$, $\mathbf{Q}$, and $\mathbf{R}$ for MPC are explicitly obtained by (1.57) and (1.63).

The obtained MPC-FBR results such as the control forces, velocities of the buoy, and the mean power capture are given in the next chapter (Chapter 2).

It is noted that since (1.70) has three state variables (z,v,$\dot{v}$), we should again employ a simplified plant model, but now of a third order. In the simplified model, the input is the control signal and the outputs are z, v, and $\dot{v}$. The state-space representation in a controllable canonical form is given by (1.65) with the state vector $\boldsymbol{x}(t) = [z(t)\ v(t)\ \ \dot{v}(t)]'$. The matrices in (1.65) are obtained by

$$\mathbf{A}_c = \begin{bmatrix} 0 & 1 & 0 \\ 0 & 0 & 1 \\ -721.6 & -78.64 & -46.03 \end{bmatrix}, \ \mathbf{B}_c = \begin{bmatrix} 0 \\ 55.38 \\ -2549 \end{bmatrix}, \ \mathbf{C}_c = \begin{bmatrix} 1 & 0 & 0 \\ 0 & 1 & 0 \\ 0 & 0 & 1 \end{bmatrix}, \ \mathbf{D}_c = \begin{bmatrix} 0 \\ 0 \\ 0 \end{bmatrix}. \quad (1.72)$$

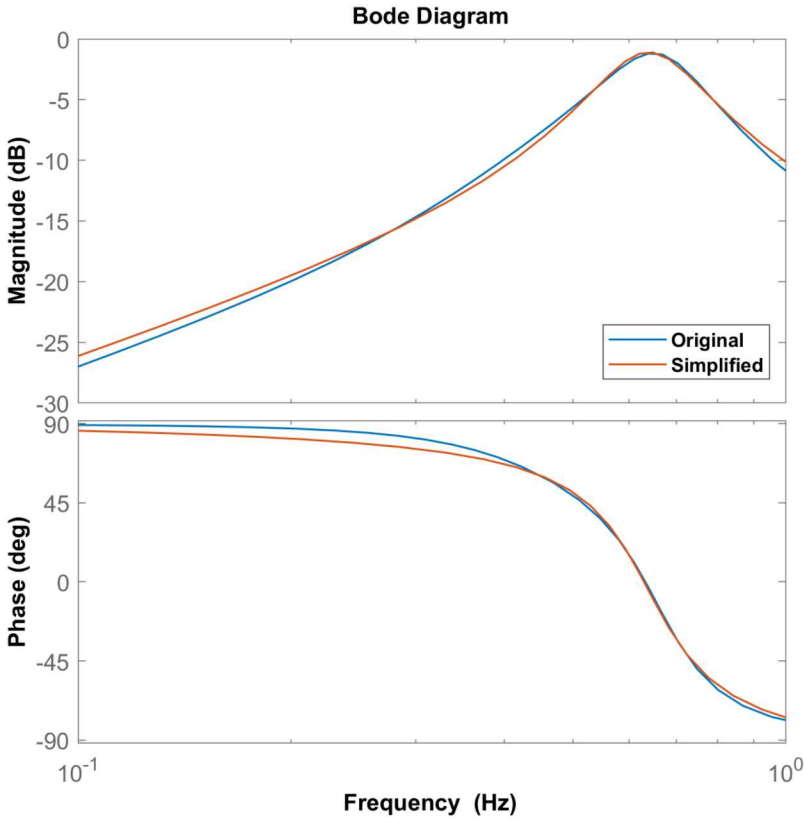

Figure 1.9: Bode diagram of the simplified (third order) and original (fourth order) models.

Its discrete-time representation is given by (1.67) with

$$\mathbf{A} = \begin{bmatrix} 1 & 0.004998 & 1.159 \times 10^{-5} \\ -0.008365 & 0.9991 & 0.004465 \\ -3.222 & -0.3595 & 0.7936 \end{bmatrix}, \mathbf{B} = \begin{bmatrix} 0.000642 \\ 0.2473 \\ -11.43 \end{bmatrix}, \mathbf{C} = \begin{bmatrix} 1 & 0 & 0 \\ 0 & 1 & 0 \\ 0 & 0 & 1 \end{bmatrix}, \mathbf{D} = \begin{bmatrix} 0 \\ 0 \\ 0 \end{bmatrix}. \tag{1.73}$$

Figure 1.9 shows the Bode diagram from the input $u(t)$ (control signal) to the output $v(t)$ obtained by the simplified model (1.72) and the original model (1.12) which has four state variables. From the figure, it is found that the simplified model matches well the original one for the frequency range of interest ($f \in [0.1\ 1.0]$).

1.6 Prediction

In the case of the "classical model" or perfect prediction the entire wave history is known ahead of time. In a realistic environment the exact wave profile acting on a WEC device will not be known. Hence, to combat the stochastic nature of the wave spectra, a few signal processing techniques will be used to estimate a model to use for the prediction. Using a given amount of current wave data each prediction method will determine its own prediction model for the wave data to run an MPC model.

1.6.1 Autoregressive (AR) model

A signal is said to be autoregressive (AR) of order p if its k^{th} sample linearly depends on its p previous samples as well as an additive white noise. An AR signal is interpreted as the output of a infinite impulse response filter (IIR) to a white Gaussian noise input. The recursive relationship of an AR model is

$$\hat{y}_k = \sum_{i=1}^{p} a_i y_{k-i} + \sigma u_k, \tag{1.74}$$

where σ^2 is the variance of the white Gaussian noise. This relationship can also be written as

$$\hat{y}_k = \boldsymbol{a}' \boldsymbol{y}_{k-1} + \sigma u_k, \tag{1.75}$$

where

$$\boldsymbol{y}_{k-1} = [y_{k-1}, \ldots, y_{k-p}]', \tag{1.76}$$

$$\boldsymbol{a} = [a_1, \ldots, a_p]'. \tag{1.77}$$

Note that $\boldsymbol{a}$ is a vector with the p coefficients that define the AR model. The optimal estimation of these coefficients can be performed through different methods such as least-squares or using the Yule-Walker equations [12]. These methods require a number of samples of the signal y as

$$\boldsymbol{y} = [y_m, \ldots, y_{m-N_d+1}], \tag{1.78}$$

where N_d is the number of samples of the signal y available. In the implementation of the AR model in this work, the $\boldsymbol{a}$ coefficients are recalculated every time a new signal sample became available. However, the number of samples used for this recalculation remains the same to N_d which means that the oldest sample is removed from the calculation once a new sample arrives.

Relation (1.74) can be interpreted as the one step prediction of the signal y. The prediction of the signal two samples into the future can be writen as

$$\hat{y}_{k+1} = a_1\hat{y}_k + a_2 y_{k-1} + a_3 y_{k-2} + \ldots + a_p y_{k+1-p}, \tag{1.79}$$

where $\hat{y}_k$ is obtained from the one step prediction in (1.74). Equation (1.79) can be written in terms of only the data available as

$$\hat{y}_{k+1} = a_1 \sum_{i=1}^{p} a_i y_{k-i} + \sum_{i=2}^{p} a_i y_{k+1-i}. \tag{1.80}$$

The prediction h-steps into the future can be expressed as

$$\hat{y}_{k+h} = \sum_{i=1}^{p} a_i \tilde{y}_{k+h-i}, \tag{1.81}$$

where

$$\tilde{y}_{k+h-i} = \begin{cases} \hat{y}_{k+h-i}, & \text{if } k+h-i \geq 0, \\ y_{k+h-i}, & \text{if } k+h-i < 0. \end{cases} \tag{1.82}$$

1.6.2 Autoregressive-moving-average (ARMA) model

To define an autoregressive-moving-average (ARMA) model it is important to first define the moving-average (MA) part. A signal is said to be represented by a MA model if it can be described by

$$\hat{y}_k = \sum_{j=0}^{q} b_j u_{k-j}, \tag{1.83}$$

where q is the order of the MA model and u_{k-j} are realizations of a white noise process. A MA signal simply is a white Gaussian noise filtered by a finite impulse response (FIR) filter.

The combination of the AR model in (1.74) with the MA model in (1.83) yields the autoregressive-moving-average (ARMA) model which can be expressed as

$$\hat{y}_k = \sum_{i=1}^{p} a_i y_{k-i} + \sum_{j=0}^{q} b_j u_{k-j}. \tag{1.84}$$

This relationship can also be written as

$$\hat{y}_k = \boldsymbol{a}'\boldsymbol{y}_{k-1} + \boldsymbol{b}'\boldsymbol{u}_k, \tag{1.85}$$

where

$$\boldsymbol{y}_{k-1} = [y_{k-1}, \ldots, y_{k-p}]', \tag{1.86}$$
$$\boldsymbol{a} = [a_1, \ldots, a_p]', \tag{1.87}$$
$$\boldsymbol{u}_k = [u_k, \ldots, u_{k-q}]', \tag{1.88}$$
$$\boldsymbol{b} = [b_0, \ldots, b_q]'. \tag{1.89}$$

Note that $\boldsymbol{a}$ is a vector of p coefficients and $\boldsymbol{b}$ is a vector of q coefficients which together define the ARMA model. An ARMA model with p coefficients for its AR part and q coefficients for its MA part is denoted ARMA(p,q). Note that if $q = 0$ it corresponds to the regular AR model of Section 1.6.1. There are multiple approaches to compute both types of coefficients one of which consists in computing the AR part as described in Section 1.6.1 and then computing those of the MA part [12]. Just like in the previous section the methods to compute the coefficients need a number of samples of the signal y as

$$\boldsymbol{y} = [y_m, \ldots, y_{m-N_d+1}], \tag{1.90}$$

where N_d is the number of samples of the signal y available. In the implementation of the AR model in this work, the $\boldsymbol{a}$ coefficients are recalculated every time a new signal sample became available. However, the number of samples used for this recalculation remains the same to N_d which means that the oldest sample is removed from the calculation once a new sample arrives.

1.6.3 Autoregressive (AR-FF) model with forgetting factor

The autoregressive (AR-FF) model with forgetting factor has the same form as the AR model as follows

$$\hat{y}_k = \boldsymbol{a}_k'\boldsymbol{y}_{k-1} + \sigma u_k, \tag{1.91}$$

where $\boldsymbol{a}_k \in \mathbb{R}^p$ is the vector with the p coefficients that describe the AR model. The estimation of these coefficients is what differentiates AR model with forgetting factor with the one described in Section 1.6.1. The generic method for this estimation is the Recursive Least Squares (RLS) algorithm with exponential forgetting factor [13]

$$\hat{\boldsymbol{a}}_k = \hat{\boldsymbol{a}}_{k-1} + P_k\boldsymbol{y}_{k-1}(y_k - \boldsymbol{y}_{k-1}'\hat{\boldsymbol{a}}_{k-1}) \tag{1.92}$$

with

$$P_t^{-1} = \lambda P_{t-1}^{-1} + \boldsymbol{y}_{k-1}\boldsymbol{y}'_{k-1}, \tag{1.93}$$

and where $\lambda \in (0,1]$ is the forgetting factor and the initial values are

$$P_0 > 0, \tag{1.94}$$

$$\hat{\boldsymbol{a}}_0 = \boldsymbol{a}_0. \tag{1.95}$$

Note that the forgetting factor λ is introduced to take into account the time-varying nature of $\boldsymbol{a}_k$ and is a parameter that usually takes values $\lambda \sim 0.95$ to 0.995. Note also that if $\lambda = 1$ the formulation above results in the standard recursive formulation of the Least Squares estimator. The prediction using this model occurs in the same way as explained in relations (1.81) and (1.82).

Chapter 2

Results

To compare all of the previous methods discussed, each method was tested against ten different wave cases with varying peak period and wave height. These results and the specific wave profiles are shown in Table 2.1. Since the complex conjugate (CC) is the analytical maximum power capture for the particular WEC device for each wave profile, each method will compare its power capture with the theoretical maximum.

Table 2.1: Power capture comparison (power shown in Watts).

#	T_p [s]	H_s [m]	γ	CC	P	PP	PI	FBR	MPC-PI	MPC-FBR	AR	ARMA	AR-FF
1	1.58	0.127	1	3.6	2.9	3.4	2.9	3.5	2.9	3.5	3.3	3.3	3.3
2			3.3	4.0	3.4	3.8	3.4	3.8	3.4	3.8	3.7	3.7	3.6
3	2.5	0.127	1	18.4	8.3	17.4	15.4	17.4	15.4	17.4	15.5	15.5	15.5
4			3.3	20.5	9.4	19.4	17.9	19.4	17.9	19.4	17.3	17.4	17.4
5		0.254	1	73.6	33.1	69.5	62.0	70.0	61.8	70.0	62.0	62.2	62.0
6			3.3	81.9	37.9	77.5	72.0	78.0	71.8	78.2	69.6	69.5	69.6
7	3.5	0.127	1	71.0	13.9	66.4	57.1	65.8	56.7	65.8	63.3	65.3	63.1
8			3.3	77.7	15.3	72.8	65.3	72.3	64.9	72.0	70.4	71.7	69.5
9		0.254	1	284.2	55.6	265.9	225.4	259.5	223.9	259.5	252.7	260.8	252.4
10			3.3	310.7	61.2	290.5	262.0	290.4	260.3	289.3	280.0	284.9	275.1

We can see from the table that the standard MPC method with perfect prediction (PP) will always outperform other prediction based MPC methods. As explained earlier, with perfect prediction the entire wave history is known. The other methods, AR, ARMA, and AR-FF, will always under perform compared to perfect prediction as we can also see from Figure 2.1.

In the case of the PI controller, using a single order estimation of the complex conjugate returns similar results with the other prediction methods. The benefit to this is that the PI controller requires no prediction, so there is no computation strain to run the PI controller in application. We see that the MPC-PI controller performs as well as the PI controller. For example, let us measure the performance by FIT (%) - the mean square error between the MPC-PI and PI control signals:

$$FIT = (1 - NRMSE) \times 100, \tag{2.1}$$

where the term *NRMSE* is defined as

$$NRMSE = \frac{\|u_{\text{PI}} - u_{\text{MPC}}\|_2}{\|u_{\text{PI}} - \bar{u}_{\text{PI}}\|_2}, \tag{2.2}$$

where u_{PI} is the control signal created by the PI controller, $\bar{u}_{\text{PI}}$ is the mean value of u_{PI}, and u_{MPC} is the control signal calculated by the MPC-PI controller. For example, the FIT is calculated as 99.64% for test case #10, which verifies that the obtained MPC-PI behaves as the PI controller pretty well.

As for the FBR method, we can see that this higher order model improves the complex conjugate estimation and has the best power captures of all the methods. This implies that using an FBR feedback controller will outperform any realizable MPC controllers as only a few cases of the perfect prediction perform better. For these specific cases, $f_p = 0.2857$ Hz, the peak period of the wave is far away enough from the devices resonant frequency $f_r = 0.6667$ Hz. Due to this, any frequency band that does not expand out to the resonant frequency will not properly capture the device dynamics. To accommodate for this the frequency band needs to cover a larger frequency band and as such the overall performance of the FBR will start to suffer. Even with this issue, the FBR performed less than a percent of the MPC perfect prediction model. Also, it is seen that the designed MPC-FBR controller exactly behaves as the FBR controller. More specifically, the FIT of the MPC-FBR control signal is calculated as 99.35% compared with that of the FBR controller for test case #10.

Figure 2.2 - Figure 2.7 display the power spectral density obtained by the CC, PI, FBR, and P (damping) controllers for test cases #1, #2, #5, #6, #9, and #10, respectively. The wave forces are also presented and the average power capture for each controller is specified in the legend for reference. As seen from the figures, all the controllers make a similar shape with the wave profile; the power is absorbed the most at the frequency at which the wave force has its peak. Also, the power captured by the CC lies in a broader range of frequencies than the other controllers, especially in low frequencies . The FBR shares a similar shape with the CC and the PI captures a little less power than the CC or the FBR. The P controller absorbs the least amount of power. As expected, the waves with smaller γ have a broader range of frequencies, and hence, the corresponding controllers absorb power from this broad frequency band. For example, compare Figure 2.4 ($\gamma = 1$) with Figure 2.5 ($\gamma = 3.3$).

In order to clearly see that the FBR controller covers a broader range of frequencies than the PI or the P controllers, Figure 2.2 - Figure 2.7 are reused to plot the power ratio; the power captured by the PI, FBR, and P controllers is divided by the power captured by the CC controller (theoretical maximum) for each frequency. The results are presented in Figure 2.8 - Figure 2.13, clearly showing that the FBR captures almost as much power as the CC, from a broader range of frequencies than the PI or the P controllers. The efficiency of the PI controller is high only in a narrow frequency band and the P controller absorbs the least power among the three.

Figure 2.14 shows the time history of the control signals for test case #10 created by the MPC with perfect prediction (PP), PI, and FBR controllers, and Figure 2.15 is a zoomed-in figure for the time range [300,400] for a clear view. It is seen that the three control signals are in phase on the whole. More specifically, the MPC with PP and the FBR controller share a similar profile and

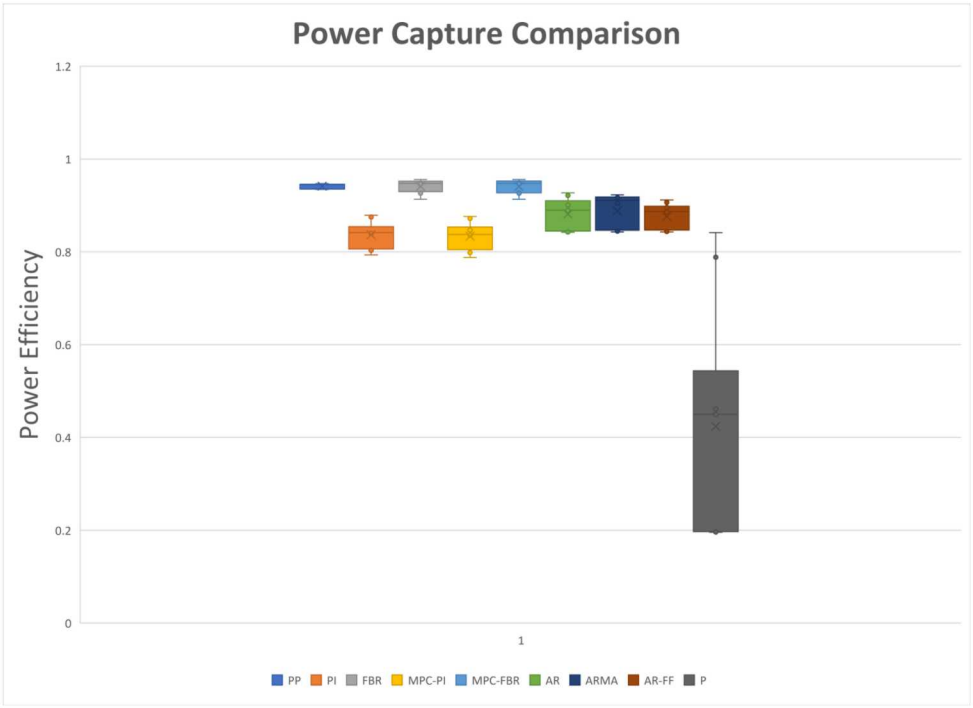

Figure 2.1: Power Capture comparison with each control method.

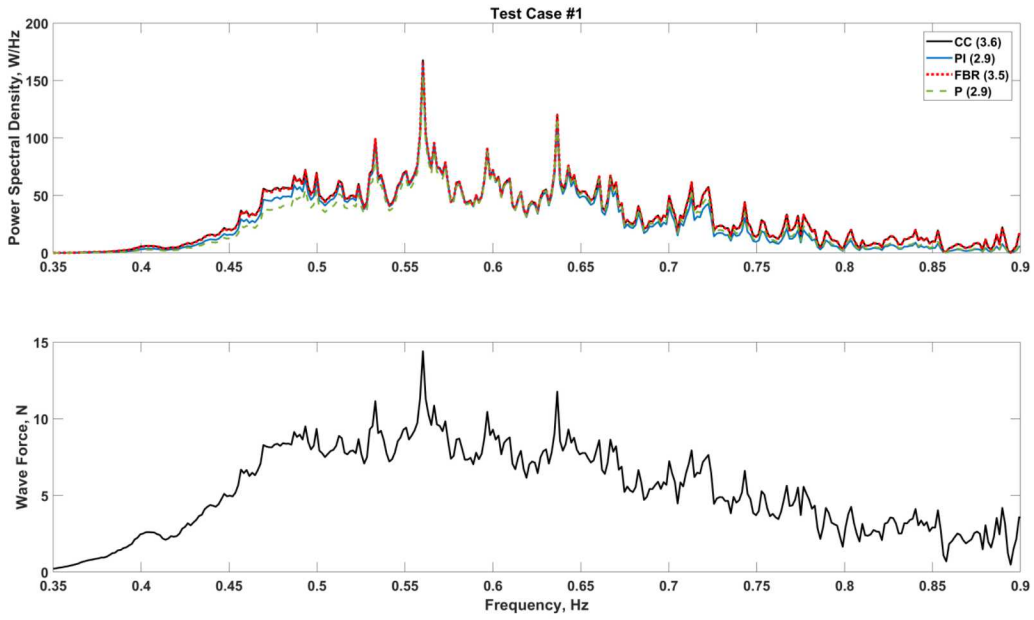

Figure 2.2: Power spectral density obtained by CC, PI, FBR, and P controllers for test case #1.

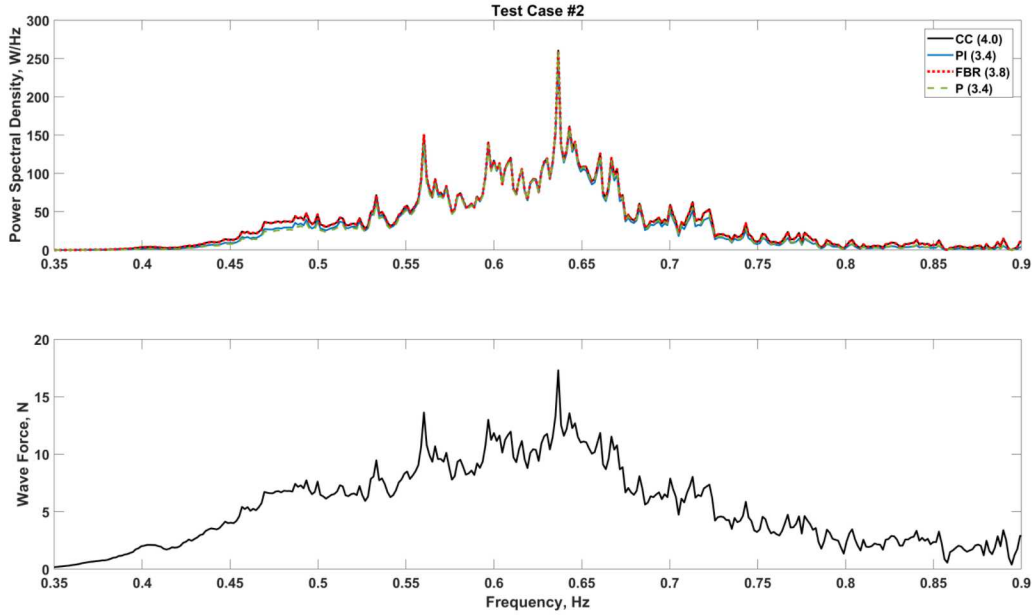

Figure 2.3: Power spectral density obtained by CC, PI, FBR, and P controllers for test case #2.

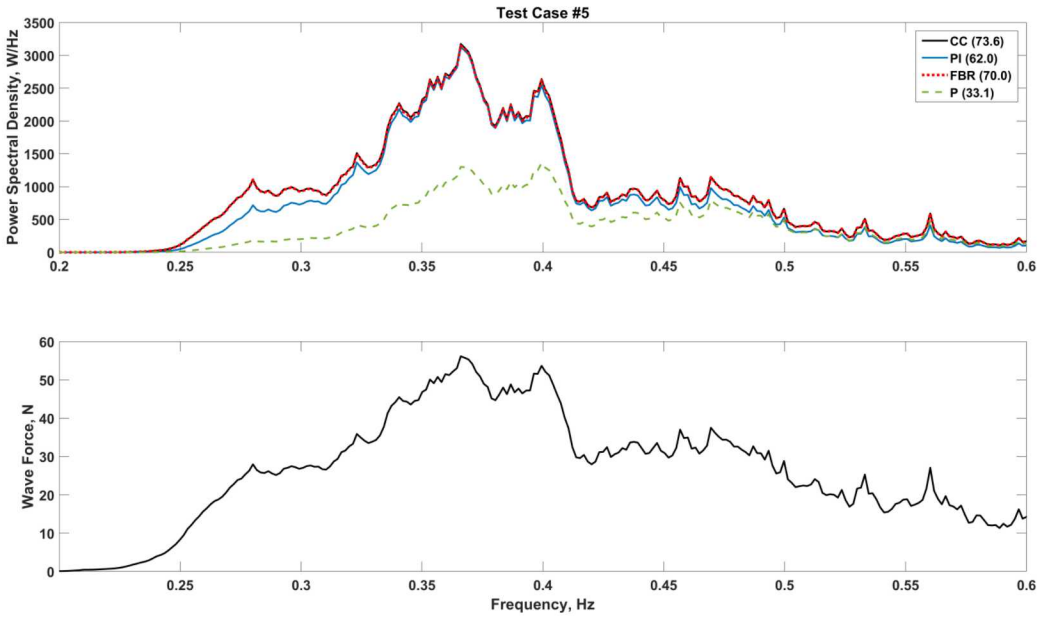

Figure 2.4: Power spectral density obtained by CC, PI, FBR, and P controllers for test case #5.

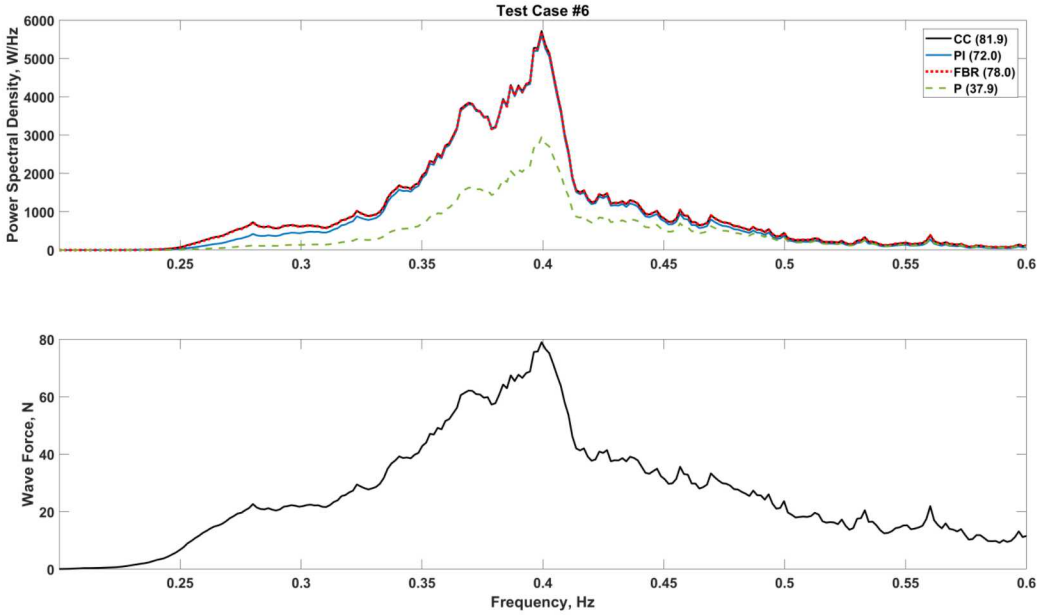

Figure 2.5: Power spectral density obtained by CC, PI, FBR, and P controllers for test case #6.

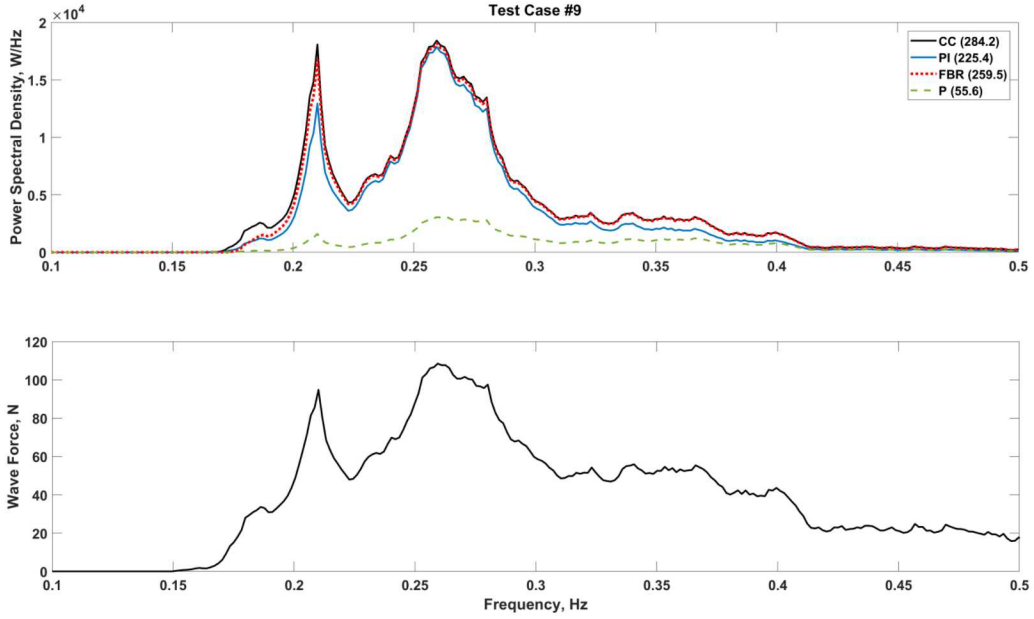

Figure 2.6: Power spectral density obtained by CC, PI, FBR, and P controllers for test case #9.

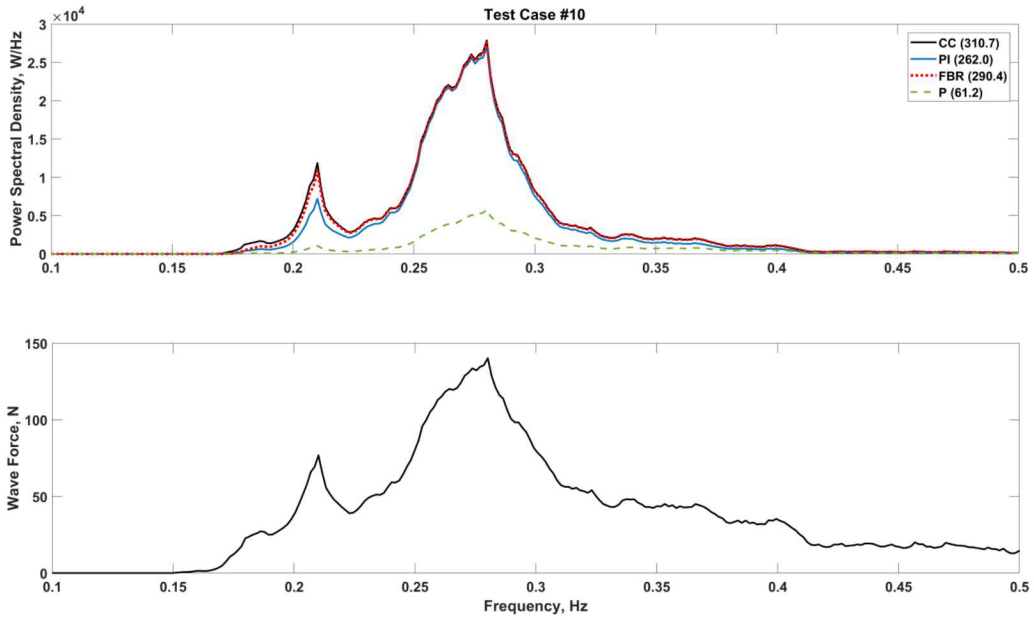

Figure 2.7: Power spectral density obtained by CC, PI, FBR, and P controllers for test case #10.

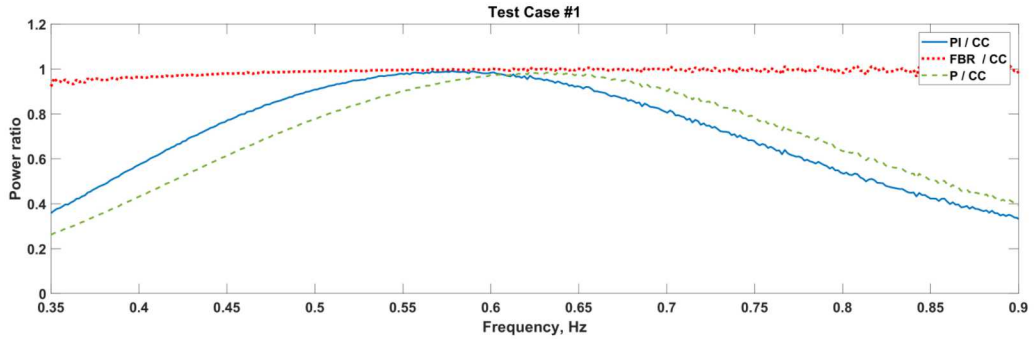

Figure 2.8: Power ratio divided by the power captured by CC for test case #1.

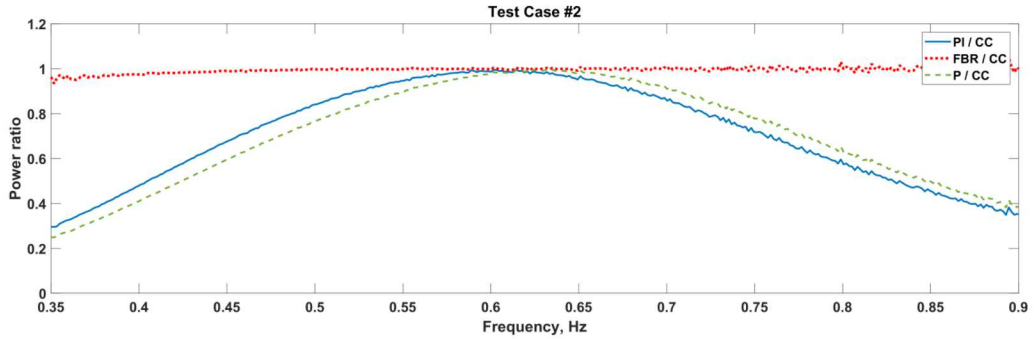

Figure 2.9: Power ratio divided by the power captured by CC for test case #2.

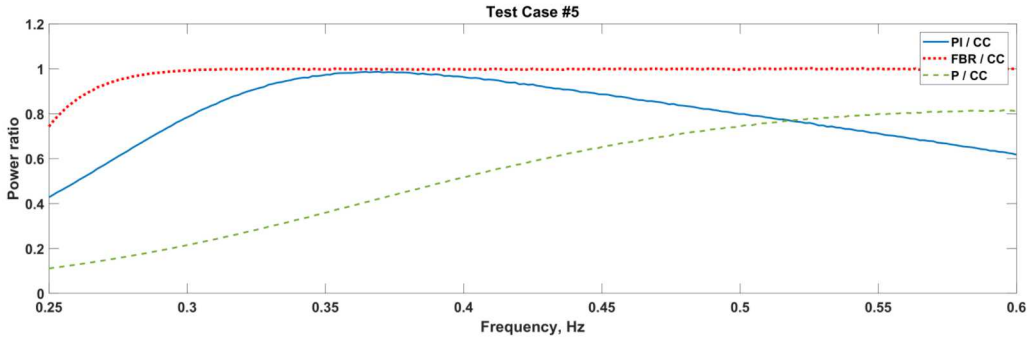

Figure 2.10: Power ratio divided by the power captured by CC for test case #5.

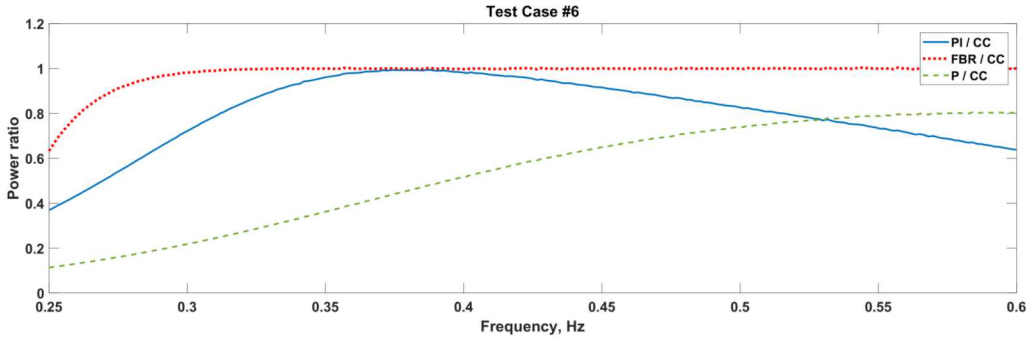

Figure 2.11: Power ratio divided by the power captured by CC for test case #6.

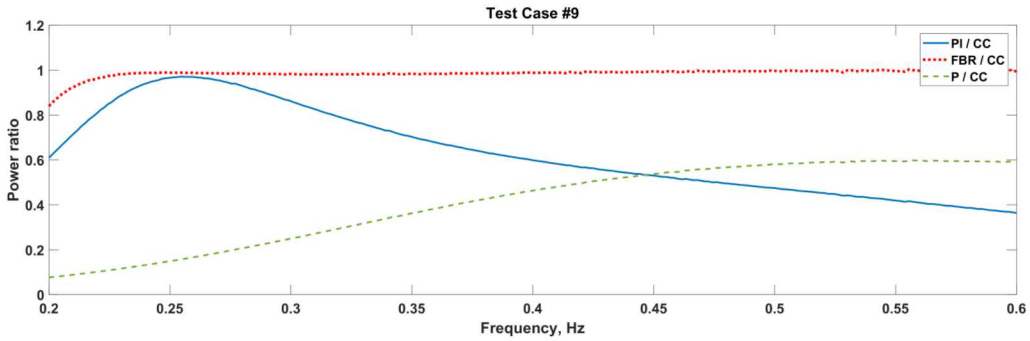

Figure 2.12: Power ratio divided by the power captured by CC for test case #9.

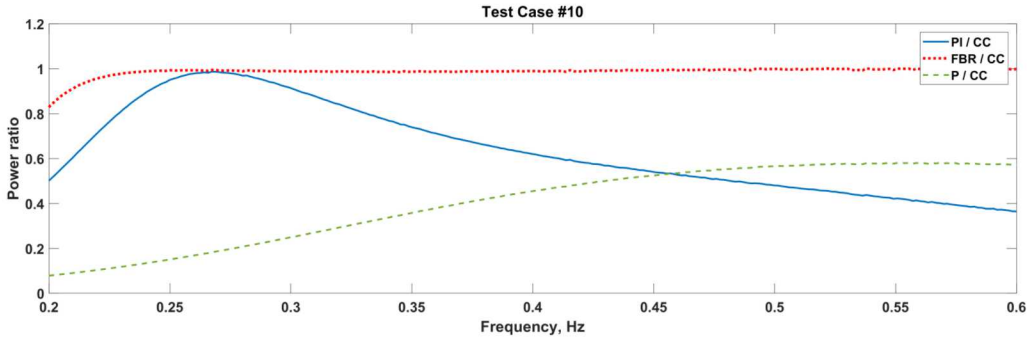

Figure 2.13: Power ratio divided by the power captured by CC for test case #10.

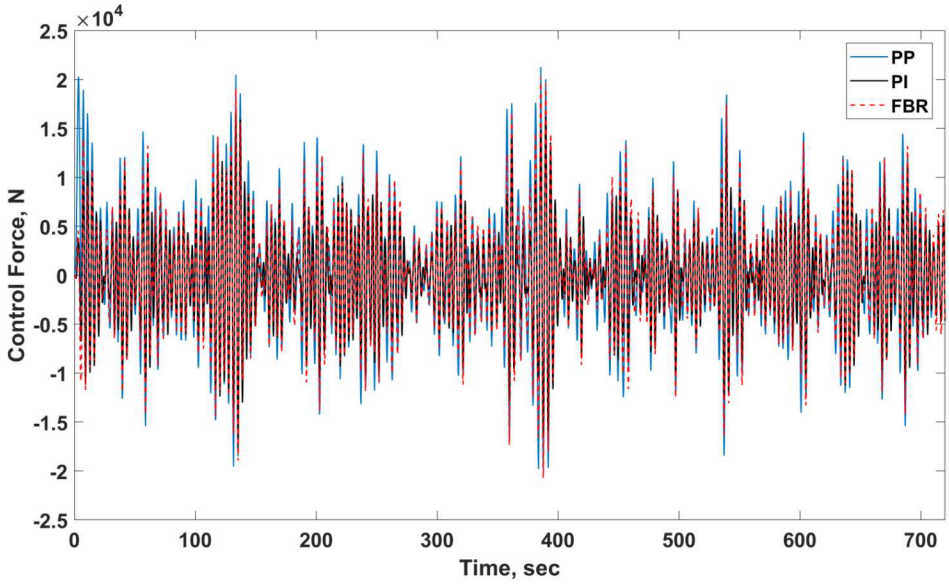

Figure 2.14: Control forces obtained by the MPC with PP, PI, and FBR controllers for test case #10.

have a little larger amplitudes, compared with the PI controller. In Figure 2.16 the time history of the velocities of the buoy for test case #10 obtained by the MPC with PP, PI, and FBR controllers is depicted, and Figure 2.17 is a zoomed-in figure for the time range [300,400]. Again, the MPC with PP and FBR controller have a similar velocity profile compared with the PI controller. Figure 2.18 displays the time history of the mechanical power for test case #10 captured by using the MPC with PP, PI, and FBR controllers, and Figure 2.19 is a zoomed-in figure for the time range [300,400]. Again, the MPC with PP and FBR controller share a similar power capture profile together, supporting the finding that the average power captured by the MPC with PP is commensurate with that captured by the FBR controller (see Table 2.1). The MPC-PI and MPC-FBR controllers yield almost the same results with the PI and FBR controllers, respectively, so their results are not shown here for brevity. The MPC-PI and MPC-FBR controllers with the constraint (control input saturation) will be designed in Appendix A and their performance will also be investigated.

Another useful metric to compare each method is the capture width, or absorption width. The capture width is defined as the ratio of the power captured to the wave-energy transport. The maximum absorption width is also related as the width equal to the wavelength of the wave divided by 2π.

As shown in Table 2.2 and Figure 2.20, the perfect prediction method and the FBR have a similar capture width as the max capture width, i.e., the complex conjugate capture width. Interestingly, we can see that the max capture width for this particular WEC device is at larger peak frequencies. As the peak frequency for the wave spectra increases, the WEC device has a better capture width for the incoming waves.

In conclusion, as we can see from comparing the causal realization methods to the standard

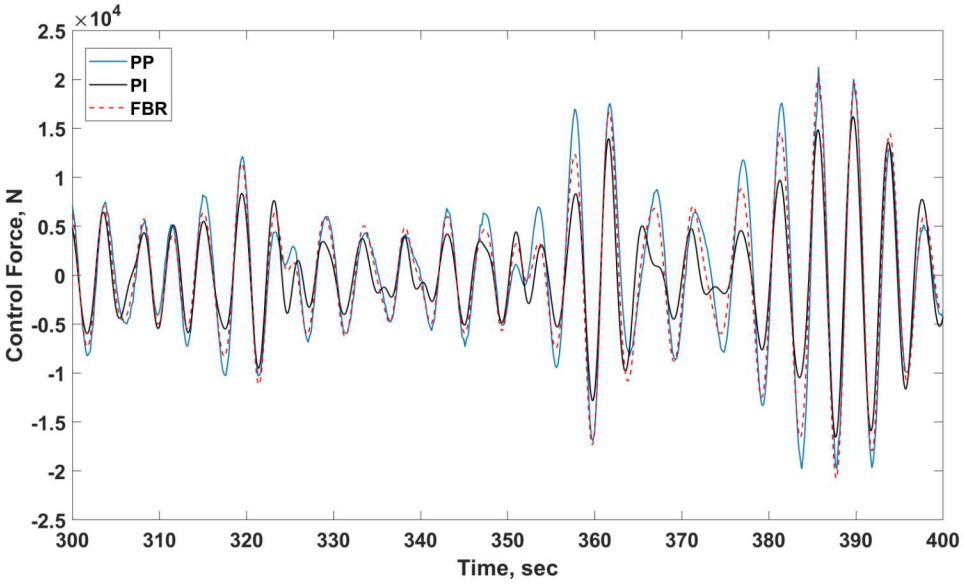

Figure 2.15: Control forces obtained by the MPC with PP, PI, and FBR controllers (zoomed in).

MPC methods, the causal realization methods perform better if not the same as the standard MPC. The major benefit to using these causal realization methods is that there is no prediction involved with determining these controllers. Due to the removal of the prediction strain, there is less dependence and the computational strain of estimating and optimizing over a particle wave history to a device.

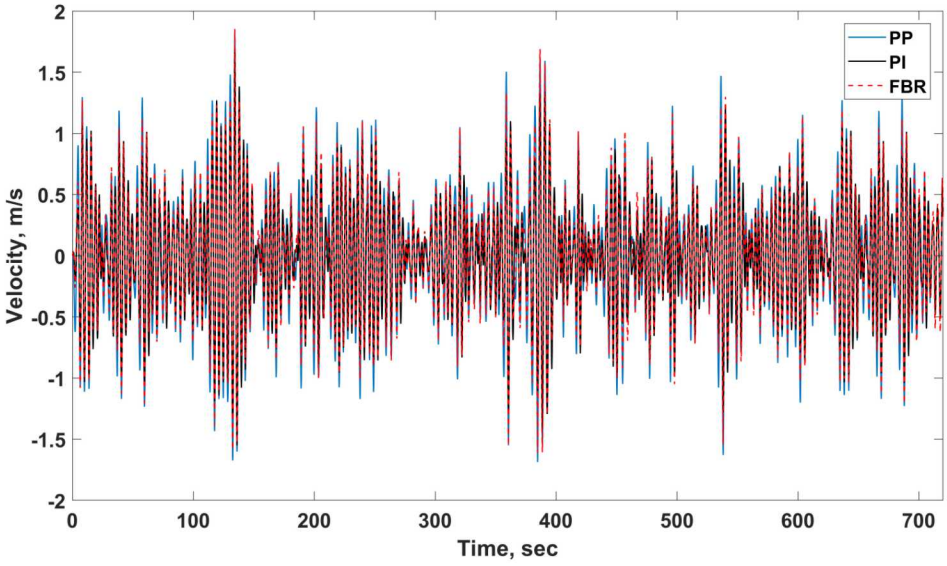

Figure 2.16: Velocities obtained by the MPC with PP, PI, and FBR controllers for test case #10.

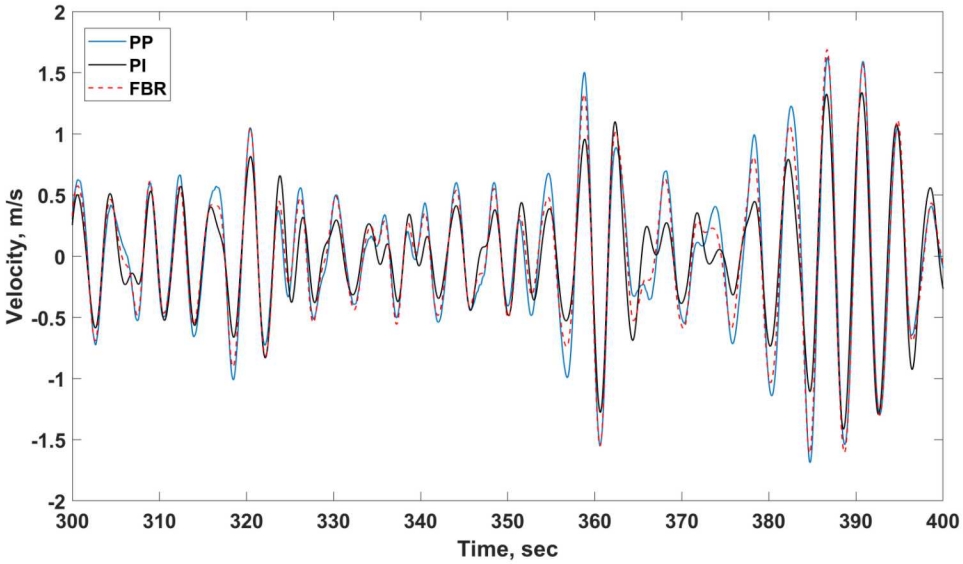

Figure 2.17: Velocities obtained by the MPC with PP, PI, and FBR controllers (zoomed in).

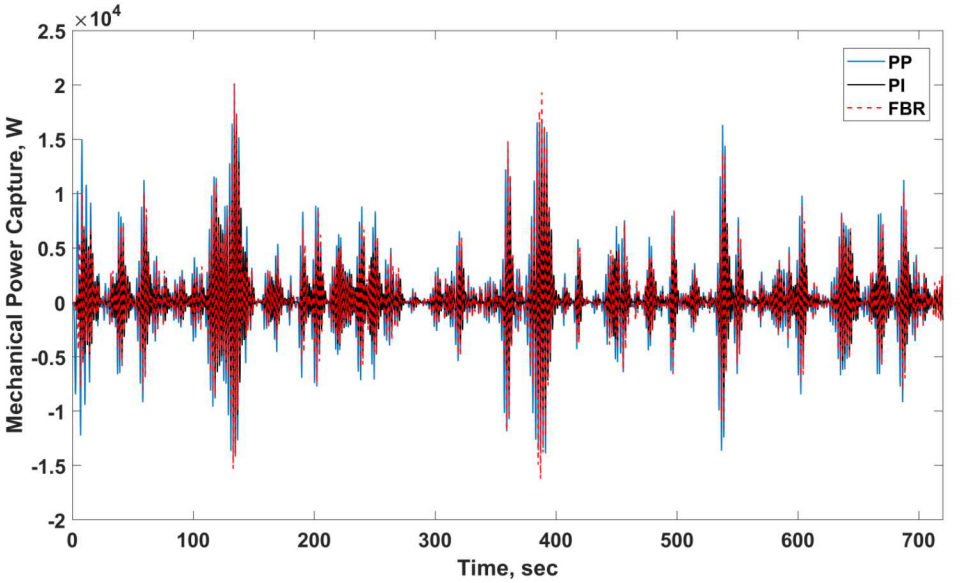

Figure 2.18: Mechanical power captured by using the MPC with PP, PI, and FBR controllers for test case #10.

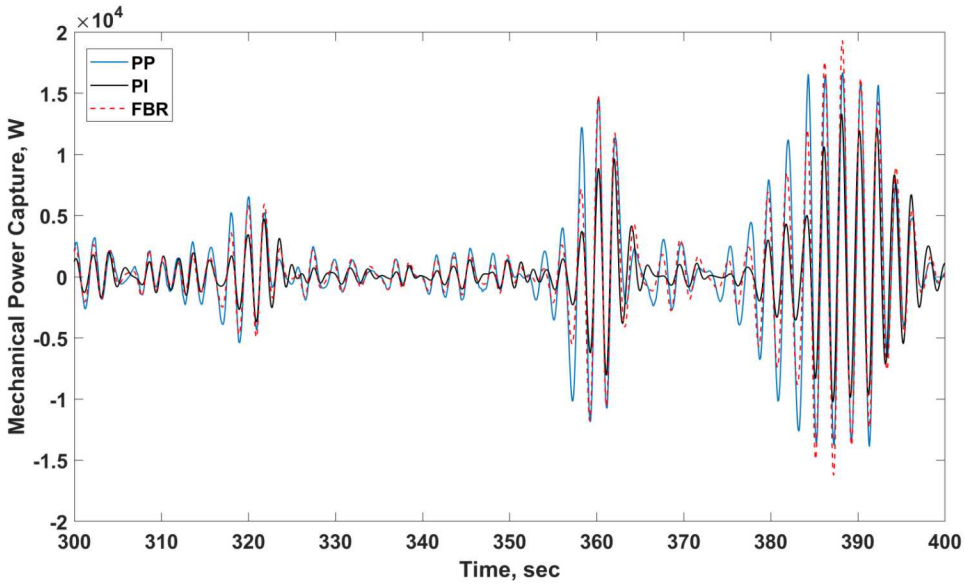

Figure 2.19: Mechanical power captured by using the MPC with PP, PI, and FBR controllers (zoomed in).

Table 2.2: Capture width comparison.

#	T_p [s]	H_s [m]	γ	CC	PP	P	PI	FBR	MPC-PI	MPC-FBR	AR	ARMA	AR-FF
1	1.58	0.127	1	0.087	0.083	0.068	0.070	0.083	0.070	0.083	0.080	0.079	0.080
2			3.3	0.091	0.086	0.076	0.077	0.087	0.077	0.087	0.084	0.083	0.082
3	2.5	0.127	1	0.279	0.263	0.124	0.234	0.264	0.233	0.264	0.235	0.235	0.235
4			3.3	0.294	0.278	0.135	0.257	0.279	0.257	0.279	0.249	0.249	0.249
5		0.254	1	0.279	0.263	0.124	0.235	0.265	0.234	0.265	0.235	0.235	0.235
6			3.3	0.294	0.278	0.135	0.259	0.280	0.258	0.281	0.250	0.250	0.250
7	3.5	0.127	1	0.768	0.718	0.150	0.617	0.712	0.613	0.712	0.684	0.707	0.683
8			3.3	0.797	0.746	0.156	0.670	0.742	0.666	0.739	0.722	0.735	0.713
9		0.254	1	0.768	0.719	0.149	0.610	0.702	0.606	0.702	0.683	0.705	0.682
10			3.3	0.797	0.745	0.156	0.672	0.745	0.667	0.742	0.718	0.731	0.706

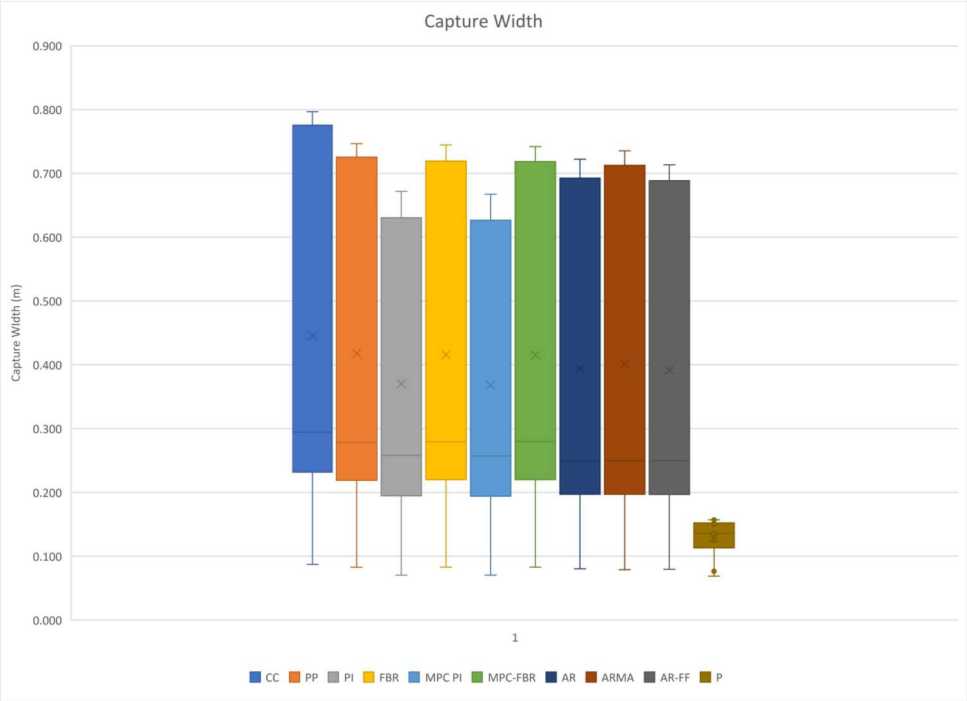

Figure 2.20: Comparison of capture width of various methods.

Chapter 3

Conclusions

This report studies a key question in wave energy control research: the need for and benefit of wave prediction/forecasting. While the study utilizes a single specific device to perform a quantitative comparison, the results will likely be similar in all resonant WEC devices. In summary, the results of this study show a very limited benefit to implementing wave prediction; feedback based controllers are capable of providing nearly the same performance without the added complication.

Additionally, it is important to note that while the prediction algorithms studied here performed relatively well, this scenario studied was highly simplified. The details of real-world implementation for such a system, including sensor selection, wave spreading, and noncollocation, are much more complicated and likely to cause a degradation in performance. Thus, the results shown here for control strategies requiring prediction (PP, AR, ARMA, and AR-FF) represent something of a best-case-scenario.

Given this consideration, the performance of the feedback-only controllers (PI, FBR, MPC-PI, and MPC-FBR) is even more attractive. These controllers require only signals/sensors which are readily available (position/velocity). Additionally, by incorporating the PI and FBR control designs within MPC frameworks, the ability to incorporate constraints is maintained as shown in Appendix A.

References

[1] K. Ogata, *Modern Control Engineering*. Prentice Hall, 2002.

[2] G. Bacelli, R. G. Coe, D. Patterson, and D. Wilson, "System identification of a heaving point absorber: Design of experiment and device modeling," *Energies*, vol. 10, no. 10, p. 472, 2017. [Online]. Available: http://www.mdpi.com/1996-1073/10/4/472

[3] D. Wilson, G. Bacelli, R. G. Coe, D. L. Bull, O. Abdelkhalik, U. A. Korde, and R. D. Robinett III, "A comparison of WEC control strategies," Sandia National Labs, Albuquerque, New Mexico, Tech. Rep. SAND2016-4293, April 2016 2016.

[4] R. G. Coe, G. Bacelli, D. G. Wilson, O. Abdelkhalik, U. A. Korde, and R. D. R. III, "A comparison of control strategies for wave energy converters," *International Journal of Marine Energy*, vol. 20, no. Supplement C, pp. 45 – 63, 2017. [Online]. Available: http://www.sciencedirect.com/science/article/pii/S2214166917300905

[5] R. G. Coe, G. Bacelli, D. Patterson, and D. G. Wilson, "Advanced WEC Dynamics & Controls FY16 testing report," Sandia National Labs, Albuquerque, NM, Tech. Rep. SAND2016-10094, October 2016. [Online]. Available: https://mhkdr.openei.org/submissions/151

[6] G. Bacelli, S. J. Spencer, R. G. Coe, A. Mazumdar, D. Patterson, and K. Dullea, "Design and bench testing of a model-scale WEC for advanced PTO control research," in *European Wave and Tidal Energy Conference (EWTEC)*, Cork, Ireland, 2017.

[7] J. N. Newman, *Marine hydrodynamics*. Cambridge, Massachusetts: MIT Press, 1978.

[8] J. Falnes, *Ocean Waves and Oscillating Systems*. Cambridge; New York: Cambridge University Press, 2002.

[9] G. Bacelli and R. G. Coe, "WEC system identification and model validation," in *Marine Energy Technology Symposium (METS2017)*, Washington, D.C., 2017.

[10] J. A. M. Cretel, G. Lightbody, G. P. Thomas, and A. W. Lewis, "Maximisation of energy capture by a wave-energy point absorber using model predictive control," in *IFAC World Congress*, 2011.

[11] S. D. Cairano and A. Bemporad, "Model predictive control tuning by controller matching," *IEEE Transactions on Automatic Control*, vol. 55, no. 1, pp. 185–190, Jan 2010.

[12] L. Ljung, *System identification*. Upper Saddle River, NJ: Prentice Hall, 1999.

[13] L. Ljung and T. Söderström, *Theory and practice of recursive identification*. Cambridge, MA: MIT press, 1983.

Appendix A

Constrained MPC

In real-life applications, there must be various kinds of constraints on the control input and/or system output, and one strength of using MPC strategies is their capability to handle constraints. Hence, the MPC-PI and the MPC-FBR controllers with the saturation constraint on the control force (we call it MPC-PI-CON and MPC-FBR-CON respectively) are designed and their performance is provided in this appendix. It is shown that the power captured by the MPC-PI-CON and the MPC-FBR-CON is poor only by a small amount when compared with the unconstrained MPC-PI and MPC-FBR even though a short horizon $N = 2$ is employed. For both controllers (MPC-PI-CON and MPC-FBR-CON), the control force signal is saturated within the range [-10000 10000] (N).

First, to compare unconstrained/constrained MPC-PI, Figure A.1 shows the time history of the control signals generated by the PI, MPC-PI, and MPC-PI-CON controllers for test case #10, and Figure A.2 is a zoomed-in figures for the time range [350,410] for a clear view. It is seen from the figures that the constraint is well satisfied and the three curves almost overlap with each other when the constraint is not active. In Figure A.3 and Figure A.4, the time history of the velocities of the buoy obtained by the PI, MPC-PI, and MPC-PI-CON controllers is depicted. Since the control signal of the MPC-PI mimics the PI control signal pretty well, their resulting velocities are also quite similar. Also, we can see that the MPC-PI-CON yields a smaller velocity than the others when the control signal is saturated. Figure A.5 and Figure A.6 display the time history of the mechanical power captured by using the PI, MPC-PI, and MPC-PI-CON controllers. As expected, when the constraint is active, the power is less captured than when the constraint is inactive. More specifically, the power captured by each controller is 261.99 W (PI), 260.26 W (MPC-PI), and 241.37 W (MPC-PI-CON), indicating that the performance of the MPC-PI-CON is reduced by 7.26% when compared with the unconstrained MPC-PI.

Likewise, the performance of the FBR, MPC-FBR, and MPC-FBR-CON is compared for test case #10, and the control signal is again saturated within the range [-10000 10000] (N). It is seen from Figure A.7 that the constraint is well satisfied and the three curves overlap with each other when the constraint is inactive. Figure A.8 is a zoomed-in figure for the time range [350,410] for a clear view. In Figure A.9 and Figure A.10, the time history of the velocities of the buoy obtained by the FBR, MPC-FBR, and MPC-FBR-CON controllers is depicted. It is again found that the MPC-FBR-CON yields a smaller velocity when the control signal is saturated. Figure A.11 and Figure A.12 display the time history of the mechanical power captured by using the FBR, MPC-FBR, and MPC-FBR-CON controllers. As expected, less power is captured when the constraint

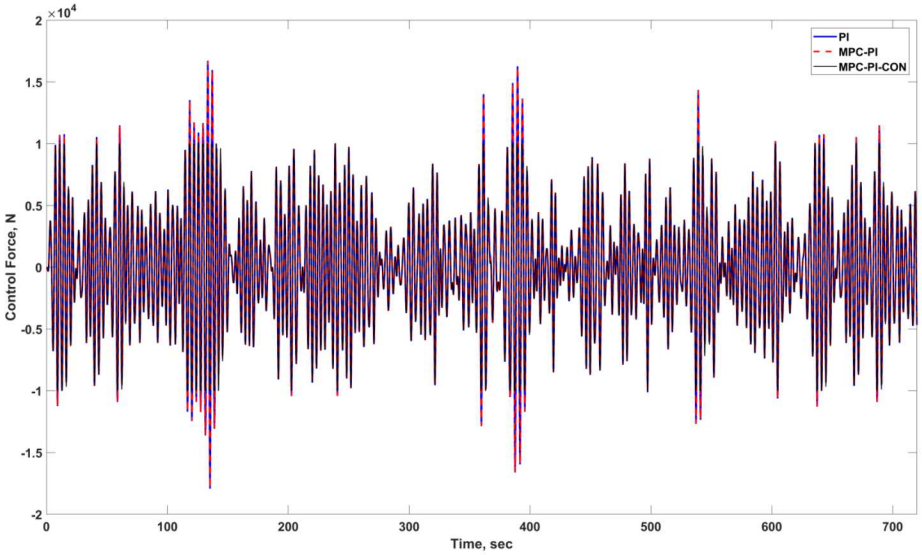

Figure A.1: Control forces obtained by the PI, MPC-PI, and MPC-PI-CON controllers.

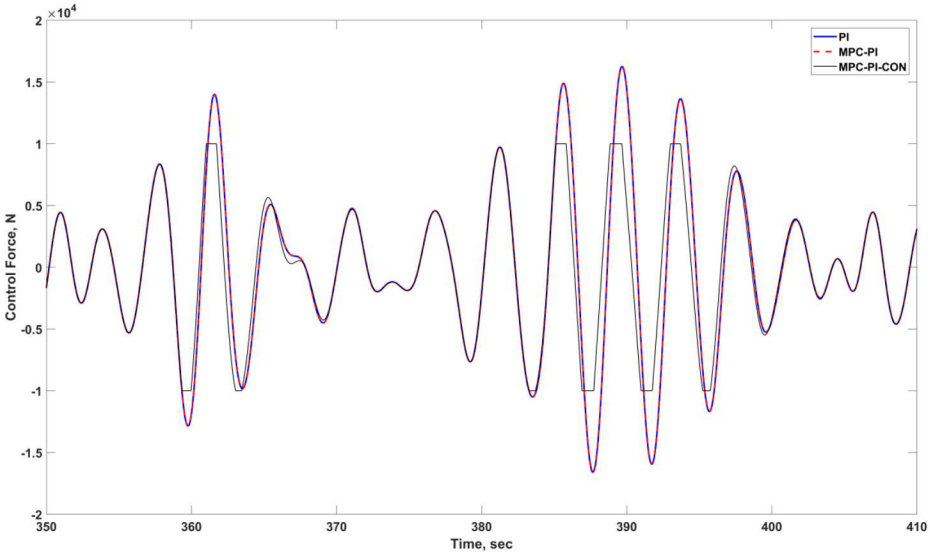

Figure A.2: Control forces obtained by the PI, MPC-PI, and MPC-PI-CON controllers (zoomed in).

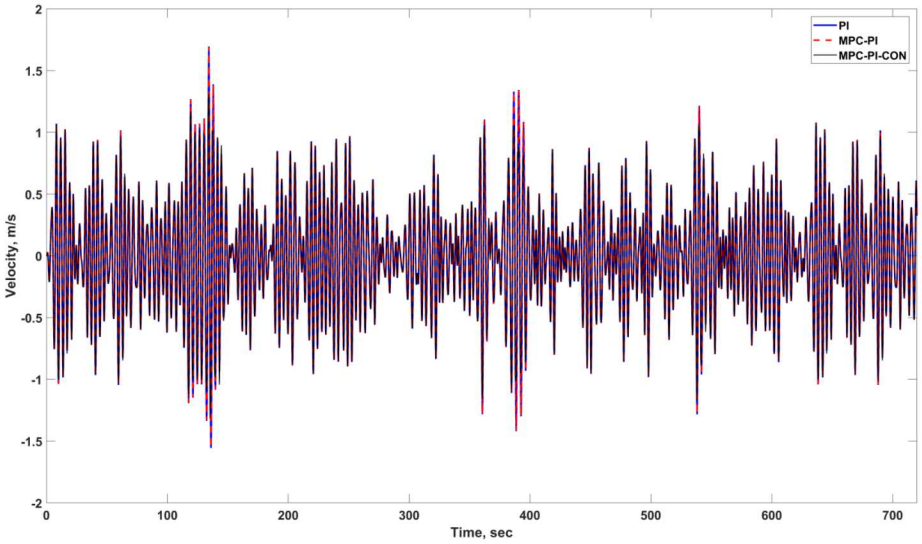

Figure A.3: Velocities obtained by the PI, MPC-PI, and MPC-PI-CON controllers.

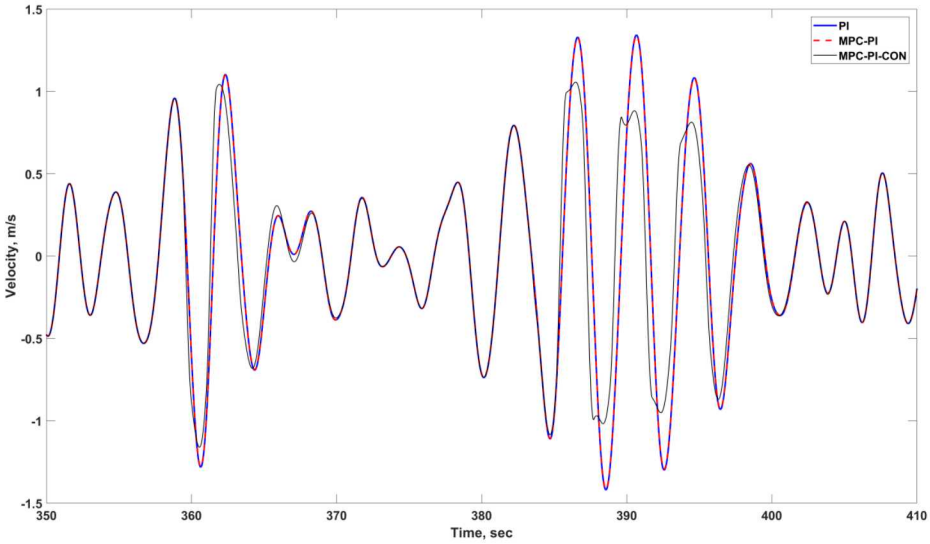

Figure A.4: Velocities obtained by the PI, MPC-PI, and MPC-PI-CON controllers (zoomed in).

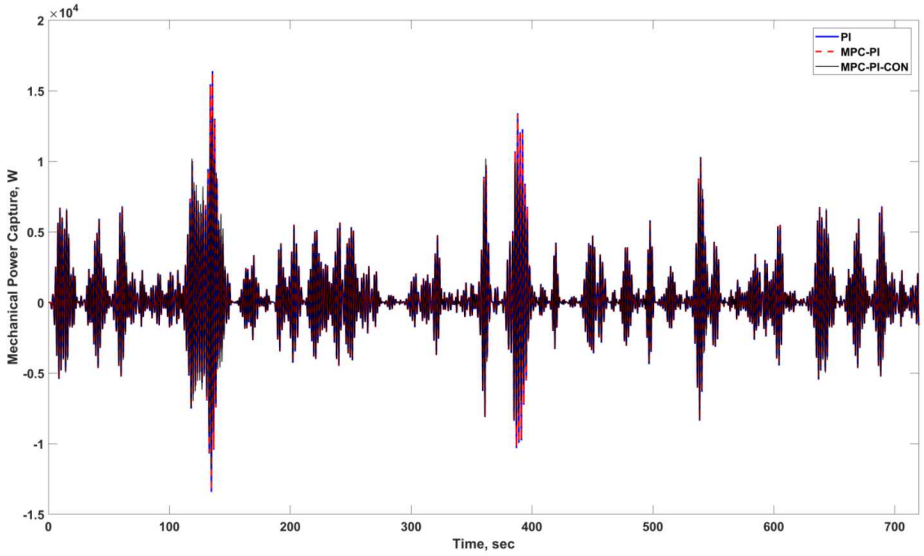

Figure A.5: Mechanical power captured by using the PI, MPC-PI, and MPC-PI-CON controllers.

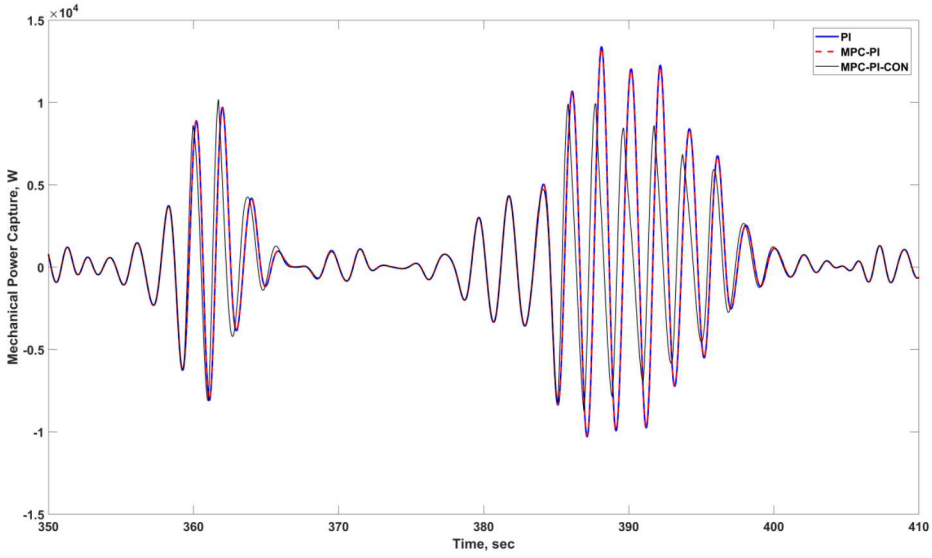

Figure A.6: Mechanical power captured by using the PI, MPC-PI, and MPC-PI-CON controllers (zoomed in).

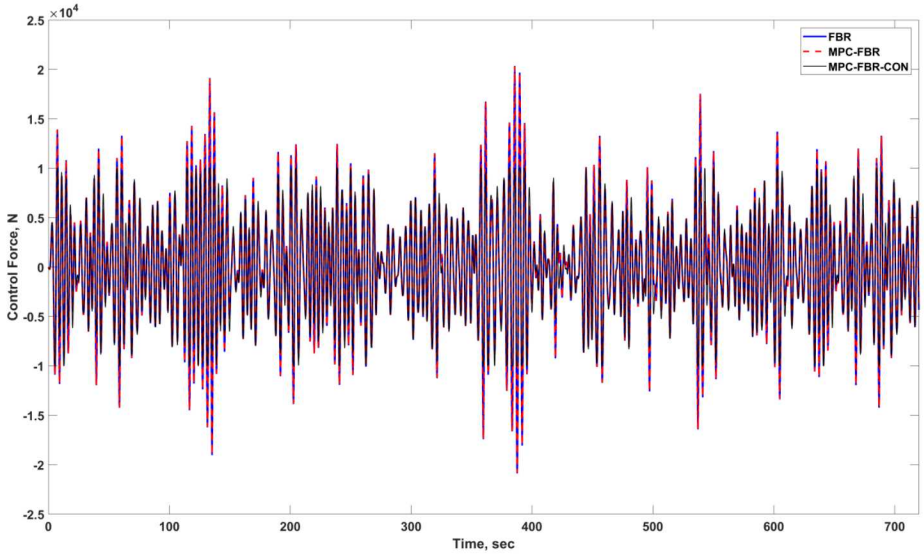

Figure A.7: Control forces obtained by the FBR, MPC-FBR, and MPC-FBR-CON controllers.

is active. More specifically, the power captured by each controller is 290.39 W (FBR), 289.32 W (MPC-FBR), and 269.25 W (MPC-FBR-CON), indicating that the performance of the MPC-FBR-CON is reduced by 7.09% when compared with the MPC-FBR.

In conclusion, the MPC-PI-CON and MPC-FBR-CON controllers with "no prediction/forecasting" could successfully handle the constraint and still maintain good power capture compared with the unconstrained cases (MPC-PI and MPC-FBR).

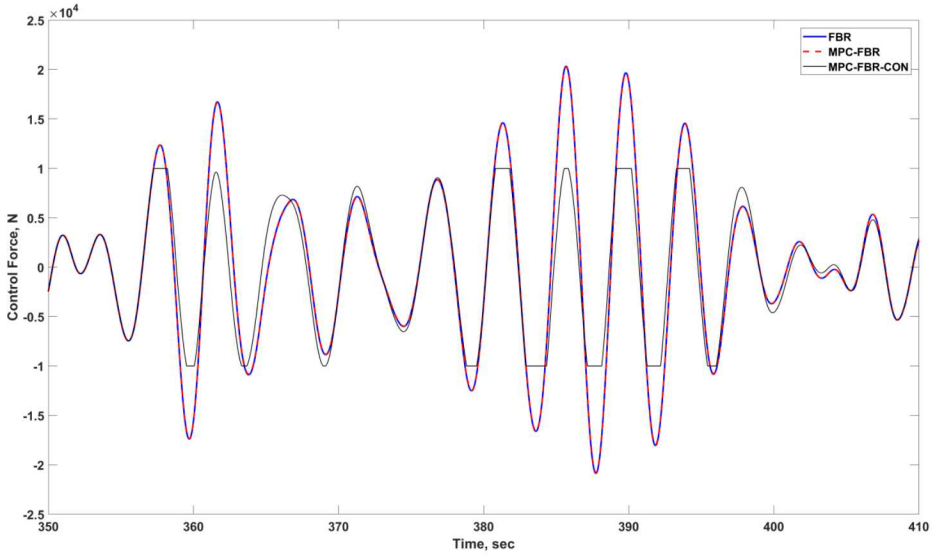

Figure A.8: Control forces obtained by the FBR, MPC-FBR, and MPC-FBR-CON controllers (zoomed in).

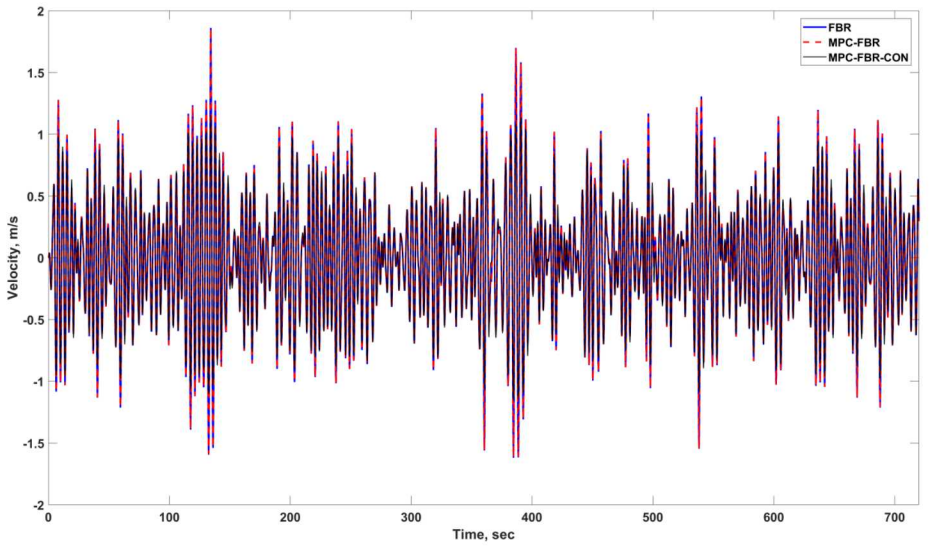

Figure A.9: Velocities obtained by the FBR, MPC-FBR, and MPC-FBR-CON controllers.

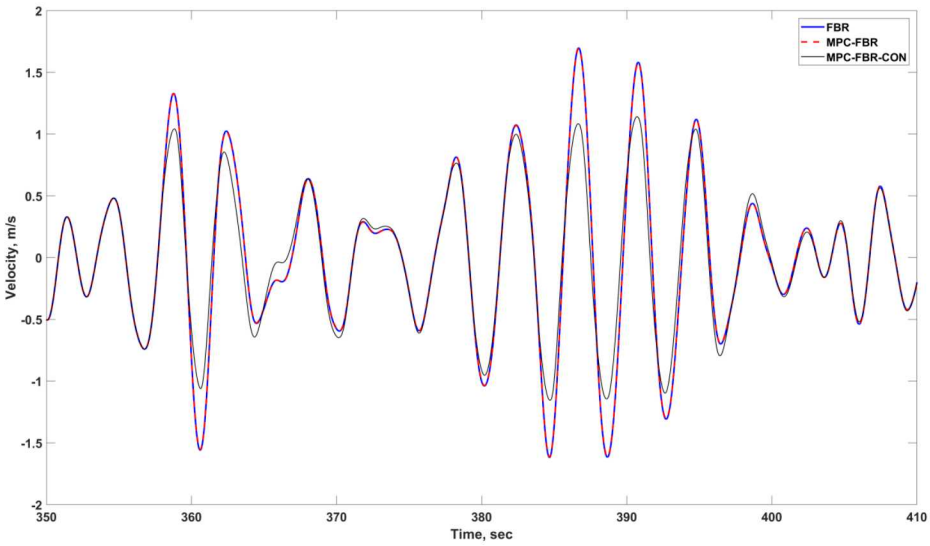

Figure A.10: Velocities obtained by the FBR, MPC-FBR, and MPC-FBR-CON controllers (zoomed in).

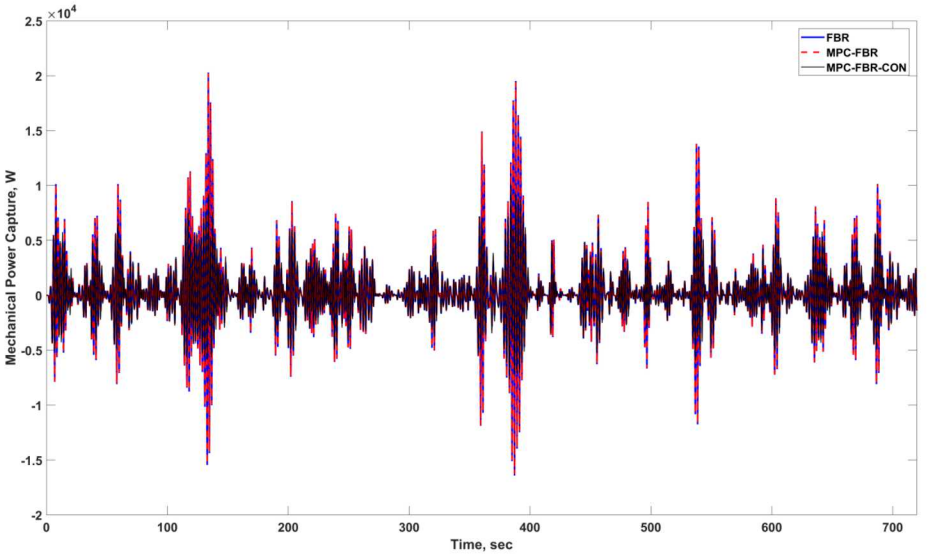

Figure A.11: Mechanical power captured by using the FBR, MPC-FBR, and MPC-FBR-CON controllers.

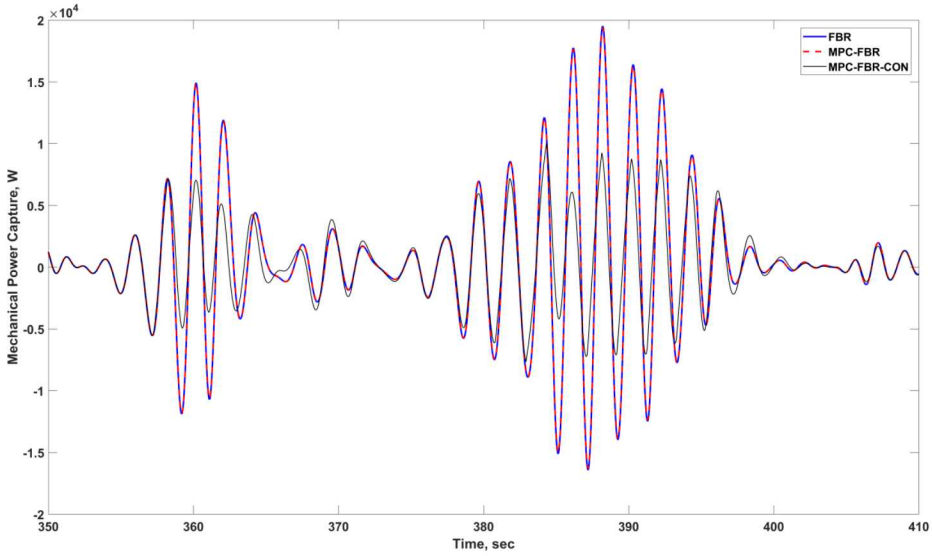

Figure A.12: Mechanical power captured by using the FBR, MPC-FBR, and MPC-FBR-CON controllers (zoomed in).

Appendix B

Prediction Sensitivity

In order to determine the optimal values necessary for the methods discussed in Section 1.6, the wave spectra were limited to peak periods away from the device's resonance and at the largest wave height. As such, the analysis will cover the wave profiles of #5, #6, #9, and #10 from Table 2.1. The sensitivity analysis will look at the response of the three prediction methods: Autoregressive, Autoregressive Moving-Average, and Autoregressive with a forgetting factor. We will be comparing the prediction results directly to MPC with perfect prediction results shown in Table 2.1.

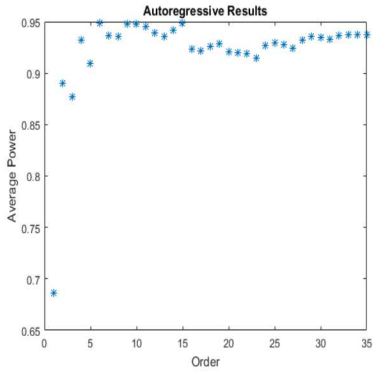

(a) Wave #10

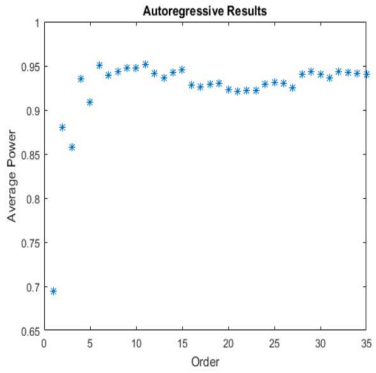

(b) Wave #9

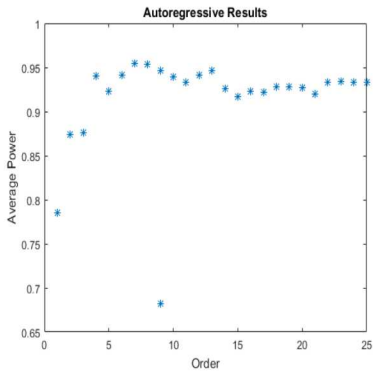

(c) Wave #6

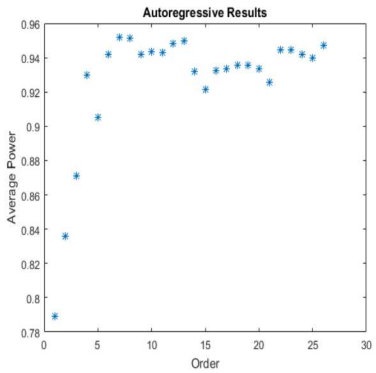

(d) Wave #5

Figure B.1: Autoregressive Responses

B.1 Autoregressive

For the Autoregressive (AR) case we are going to look at the response of the autoregressive method by solely varying the model's order. Shown in Figure B.1, we can see the overall response of the autoregressive to be around $93\% - 95\%$ compared to the perfect prediction power output.

We can see that for all four sea states the lower orders around 5-15 have the more optimal responses. We can also see that at the lower orders the AR method has a significant power drop off. Overall at higher orders greater than fifteen the power captured starts to stabilize and does not improve at all.

Due to the fact that computational complexity increases significantly with the model's order, lower model orders are preferred in general. Due to this the range of search for an optimal model order should ideally be between 5-15. At lower orders the quality of response is too low due to the order not being large enough to model enough of the wave profile for the prediction.

B.2 Autoregressive Moving-Average

For the Autoregressive Moving-Average (ARMA) method we will look at both the prediction option and the forecast option separately. Again we will be comparing the power output with the perfect prediction power output as a reference.

B.2.1 Prediction

For the prediction results, shown in Figure B.2, we see that the overall average for the prediction method is below eighty percent. We can see that the prediction output overall performs the worst of all of the methods. However, we can see that varying the moving average order tends to increase the power output overall. We do see that there is a bit of a consistent trend for the output to improve slightly with increasing the moving average order, although the trade off can be noticed at moving average orders around 6 for various model order cases.

B.2.2 Forecast

For the forecasting results, shown in Figure B.3, we see some more consistent responses. In both ARMA methods we see the highest responses from orders 21-25 but an immediate drop off to the worst response with the lower orders performing more consistent. On average the forecast method is performing around $94\% - 95\%$. We see that this performance is slightly better than the autoregressive but at different order levels.

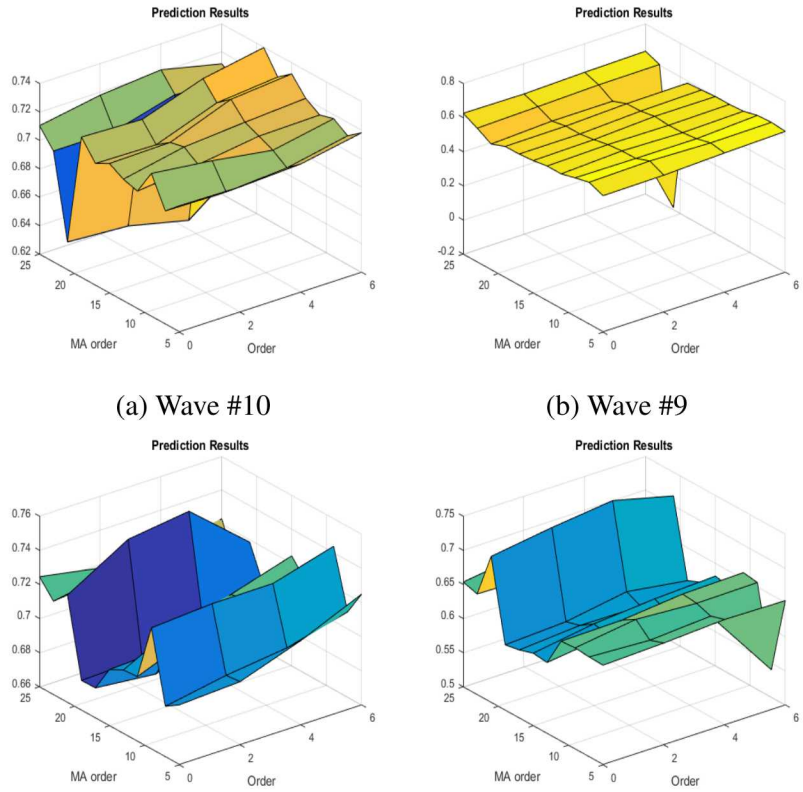

(a) Wave #10

(b) Wave #9

(c) Wave#6

(d) Wave #5

Figure B.2: Autoregressive ARMA Prediction

The optimal values for the ARMA case using the forecasting prediction seem to be around model order of 25 and using a moving average of 5 for the prediction. For determining the optimal ARMA case we plan on using only forecasting as it outperforms the prediction case in all model orders and moving average orders.

B.3 Autoregressive with Forgetting Factor

As for the autoregressive with forgetting factor (AR-FF) method, shown in Figure B.4, we can see that the power output average is around 0.92. We can also see that as the forgetting factor slowly increases the power output slightly increases. There are however, some noticeable orders where the forgetting factor tends to lose power capture. Similar to the responses for the AR method, the lowest orders below five have terrible power captures and some are even losing power. Also similar are the orders and shift in overall response of the orders with respect to optimal power capture.

Overall we can observe that the order trends from the AR method translate well over to the recursive method. As for choosing the forgetting factor, on average just using the largest forgetting factor normally improves power capture but there are some noticeable cases where this trend is

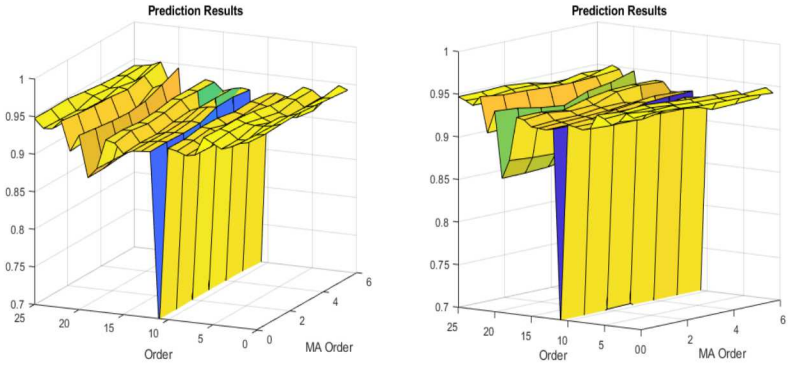

(a) Wave #10

(b) Wave #9

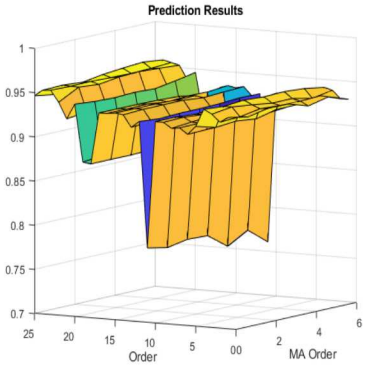

(c) Wave #6

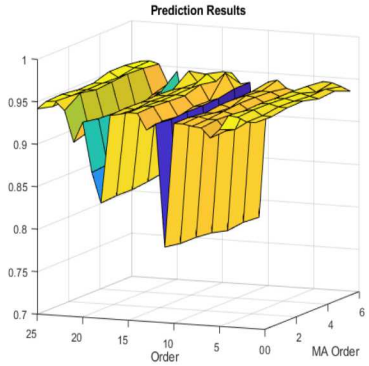

(d) Wave #5

Figure B.3: Autoregressive ARMA Forecast

not followed. The major drawback of increasing the forgetting factor is again the computational complexity coupled with the model's order. As the overall increase in power output is not enough to justify the larger computational load on the prediction, using the forgetting factor of 0.99 is sufficient.

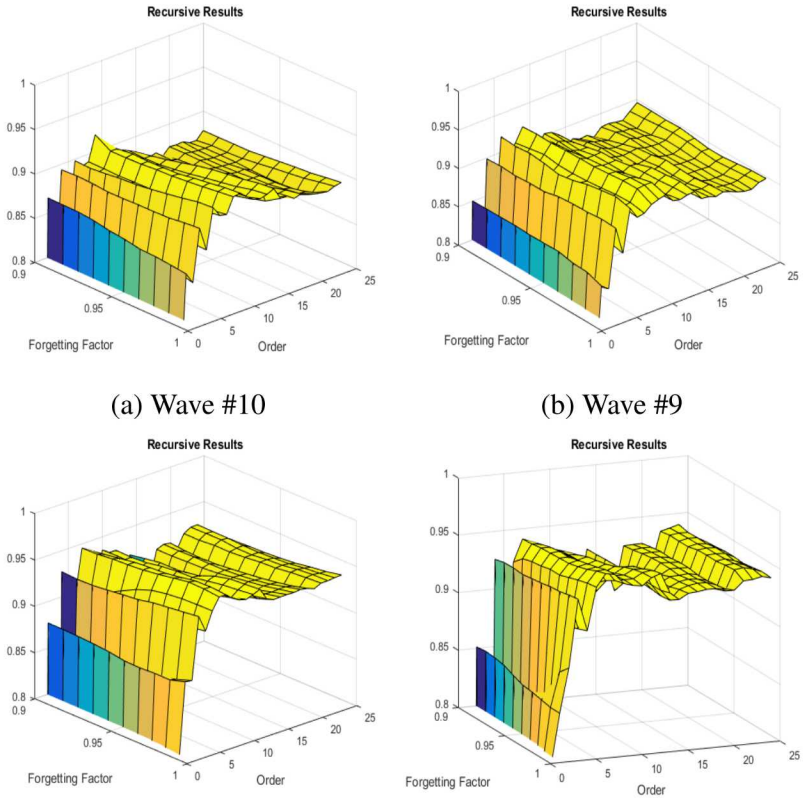

(a) Wave #10

(b) Wave #9

(c) Wave #6

(d) Wave #5

Figure B.4: Autoregressive with Forgetting Factor


Sandia National Laboratories